Mechatronics 100 (2024) 103169

Contents lists available at ScienceDirect

Mechatronics

journal homepage: www.elsevier.com/locate/mechatronics

Nondimensional analysis and experimental assessment of the $PII^{1/2}DD^{1/2}$ position control of a rotary axis

Luca Bruzzone [a,*], Chiara Micheli [b]

[a] Mechanical, Energy, Management and Transport Engineering Department (DIME), University of Genoa, Italy

[b] Electrical, Electronics and Telecommunication Engineering and Naval Architecture Department (DITEN), University of Genoa, Italy

ARTICLE INFO

Associate Editor: Prof Chris Manzie

Keywords:
Fractional order control
Distributed order PID
$PII^{1/2}DD^{1/2}$ control
Fractional calculus
Mechatronic axis

ABSTRACT

Fractional Order controllers, based on derivatives and integrals of non-integer order, represent a propitious and promising research area since they can improve the performance of mechatronic systems compared to traditional Integer Order PID controllers without requiring hardware upgrades, but only using their higher tuning flexibility. Nevertheless, Fractional Order controllers are still rarely applied in real automation tasks, since their tuning is more complex and in general requires a model-based optimization for full exploitation of their capabilities. Recently, the $PII^{1/2}DD^{1/2}$ controller has been proposed, extending the classical PID by introducing a half-integral and a half-derivative term. A Bode plot-based tuning method has been presented for this controller, deriving the $PII^{1/2}DD^{1/2}$ parameters from a given set of PID gains. This method enables a significant reduction in tracking error for position control of a mechatronic axis without the need for complex model-based optimizations. In this paper, the previous results of this $PII^{1/2}DD^{1/2}$ tuning methodology have been generalized by employing a nondimensional approach. This approach highlights the conditions under which the benefits of this Fractional Order controller over the PID are most significant. The findings have been validated through experimental tests on a rotary axis, confirming the correctness and usefulness of the method.

1. Introduction

The branch of mathematics known as Fractional Calculus (FC) extends the concepts of derivatives and integrals to non-integer orders [1]. This extension was already considered and investigated by De L'Hopital, Leibniz, Euler, Fourier, Liouville, and Riemann [2]. However, FC was forgotten for a long period and then rediscovered in the last few decades. Nowadays, FC is widely used for modelling in physics [3], mechanics [4], and biology [5]. Fractional Order (FO) equations are widely used to model multi-scale phenomena, such as viscoelasticity [6] or the evolution of the COVID-19 pandemic [7], providing better accuracy than Integer Order (IO) models.

Besides being a powerful modelling tool, FC is broadly used in engineering applications, especially in control system design. Most control schemes use IO derivatives and integrals of the error. Consequently, the adoption of FO derivatives and integrals allows an increase in the number of control parameters that can be tuned to improve the closed-loop behaviour, for example through the well-known $PI^{\lambda}D^{\mu}$ scheme, where the integral and derivative terms have non-integer orders λ and μ [8].

Practical applications, tuning criteria, and performance benefits of the $PI^{\lambda}D^{\mu}$ controller over the PID have been extensively debated in the literature [9]. For example, FO extensions of the isodamping approach [10] and of the Astrom–Hagglund and Ziegler–Nichols methods [11] have been proposed. Other researchers have applied optimization techniques to the $PI^{\lambda}D^{\mu}$ scheme, such as Particle Swarm Optimization [12], Artificial Bee Colony algorithms [13], Sine–Cosine Algorithms [14], optimal shaping of the Bode plot [15], and optimal design in the v-domain [16].

Focussing on motion control, $PI^{\lambda}D^{\mu}$ can improve the transient behavior of mechatronic devices actuated by different types of electrical motors: DC motors [17–22], permanent magnet synchronous motors [23,24], linear motors [25,26], and linear positioning systems [27]. Therefore, the application of FC to control mechatronic devices can be considered an effective instrument to enhance their performance. This can be pursued either independently or in combination with other advanced techniques, such as adaptive robust control [28,29] and model-based friction compensation [30].

This paper was recommended for publication by Associate Editor Prof Chris Manzie

[*] Corresponding author.
E-mail address: luca.bruzzone@unige.it (L. Bruzzone).

https://doi.org/10.1016/j.mechatronics.2024.103169

Even if the $PI^{\lambda}D^{\mu}$ scheme is the most common approach to applying FC to control system design, there are several different methodologies involving FC in combination with other control techniques. For example, in [31] a FO disturbance observer is exploited to enhance the performance of sliding mode control. In [32] a FO sliding mode control based on single parameter adaptive law is used for nano-positioning of piezoelectric actuators. FO sliding mode controllers can also improve the performance of electro-hydraulic servo systems [33]. In [34], a FO filter is used in combination with a fuzzy logic system approximator and a grey wolf and weighted whale optimization algorithm. In [35], a combination of FO dynamic surface control and fault-tolerant control is used to improve the stability of systems with unknown linearities, with an application to a permanent magnet synchronous motor. In [36], a fractional sliding mode control is used to control a bearingless induction motor. In [37], a FO extended state observer is used for active disturbance rejection control and validated through the application to a cart-pendulum system actuated by a DC motor. In [38], a FO version of the reset control is exploited for motion control, with experimental tests on a positioning stage. In [39], a FO feedforward compensation method is proposed to increase the tracking accuracy of a permanent magnet linear synchronous motor.

Another possible way to use FC in control system design is by adding FO terms to the PID scheme instead of replacing the IO terms. The $PDD^{1/2}$ controller is derived from the PD scheme through the introduction of the half-derivative component, based on the derivative of order 1/2. The dynamic behaviour of a purely inertial system, position-controlled using the $PDD^{1/2}$ scheme, is theoretically analysed through a nondimensional approach [40]. The PD, PD^{μ}, and $PDD^{1/2}$ position controls of second-order linear systems are compared by simulation in [41], demonstrating that the two FO schemes achieve similar performance improvements compared to the IO one and that the $PDD^{1/2}$ has slightly better readiness and slightly higher overshoot than the PD^{μ}. The effectiveness of the $PDD^{1/2}$ control was experimentally validated in application to a micrometric linear axis [42] and to a rotor [43].

While the $PDD^{1/2}$ control scheme has no integral action to eliminate the steady-state error, its $PII^{1/2}DD^{1/2}$ extension, proposed in [44], is characterized by an integral term and a half-integral term, proportional to the integral of order 1/2. It can be considered as a Distributed Order PID [45], in which the control action is given by the combination of an odd number of terms, proportional to differintegrators of the error with equally spaced orders ranging from -1 to $+1$. For the $PII^{1/2}DD^{1/2}$ scheme, the orders are five (-1, $-1/2$, 0, $+1/2$, $+1$). In [44], the formulation of the $PII^{1/2}DD^{1/2}$ control and its frequency response have been discussed, and a Bode plot-based tuning method has been proposed and tested for position control of a rotor.

In the present paper, the comparison between PID control and $PII^{1/2}DD^{1/2}$ control is carried out for the sake of generality using a nondimensional model, considering position control of a purely inertial load. This comparison enables the definition of conditions under which it is advantageous to replace the PID control with the $PII^{1/2}DD^{1/2}$ control, quantifying benefits and drawbacks.

After introducing the nondimensional model, the PID and $PII^{1/2}DD^{1/2}$ closed-loop systems are first compared numerically in the step response, providing general indications for deriving a $PII^{1/2}DD^{1/2}$ tuning form a given PID controller. The effectiveness of the proposed tuning methodology is then experimentally validated using a real system that is position-controlled with trapezoidal velocity profile. The results demonstrate that the proposed FO scheme can be easily applied to a mechatronic axis, enhancing its performance without relevant hardware modifications.

The main advantage of the proposed FO control design method is that the control parameters can be directly obtained through explicit formulas starting from a given PID controller, increasing its performance without the need for optimization, system identification, or implementation of adaptive methods. This feature is noteworthy, considering the substantial gap between the cutting edge of control design science and the real mechatronic scenario. Despite the widespread evidence that FO controllers overperform IO ones, the latter continue to dominate in the industry. Consequently, some researchers have recently proposed FO control schemes with tuning guidelines more focused on ease of implementation rather than optimal performance [46].

The remainder of the paper is organized as follows:

- Section 2 introduces the Grünwald–Letnikov definition of the differintegration operator and its discrete-time implementation;
- Section 3 outlines the formulation of the $PII^{1/2}DD^{1/2}$ controller and compares the frequency-domain responses of the PID and the $PII^{1/2}DD^{1/2}$ tuned according to the Bode plot-based criteria proposed in [44];
- Section 4 develops the nondimensional formulation of the position control of a purely inertial second-order system, deriving the dimensionless transfer functions of the PID and $PII^{1/2}DD^{1/2}$ controllers and the corresponding dimensionless closed-loop transfer functions;
- Section 5 compares, in continuous time simulation, the PID and $PII^{1/2}DD^{1/2}$ closed-loop systems in the case of step input;
- Section 6 applies the tuning indications obtained in the previous section to a real mechatronic axis, position-controlled by adopting a set-point with trapezoidal velocity profile;
- in Section 7, the comparison is extended to include the $PI^{\lambda}D^{\mu}$ controller, with simulation and experimental results;
- Section 8 outlines conclusions and future work directions.

2. Fractional-Order derivatives and integrals

In FC integration and differentiation to a non-integer order are represented by the same differintegration operator ${}_aD_t^{\alpha}$:

$$
{}_aD_t^{\alpha} = \begin{cases} d^{\alpha}/dt^{\alpha} & \mathrm{Re}(\alpha) > 0 \\ 1 & \mathrm{Re}(\alpha) = 0 \\ \int_a^t (d\tau)^{-\alpha} & \mathrm{Re}(\alpha) < 0 \end{cases} \tag{1}
$$

where a and t are the time interval limits, and α is the order.

The order α can be real or complex, but in this work, we assume that it is real. With this hypothesis, the following properties hold, shared with IO derivatives and integrals:

- when a FO differintegration of order α is applied twice to a time function, the resulting function is the differintegration of order 2α;
- when applied to a sinusoidal function, a FO differintegration of order α produces a phase shift of $\alpha\pi/2$: the derivative of order 1/2 produces a $+\pi/4$ phase shift, while the integral of order 1/2 produces a $-\pi/4$ phase shift.

Several theoretical definitions of the differintegration operator have been proposed [2], but it is possible to demonstrate that they are equivalent [47]. In the following, the Grünwald–Letnikov definition is used because of its robustness for discrete-time implementation [48]. According to this definition, given a function of time $x(t)$, both its differentiation of order α (if $\alpha > 0$) and its integration of order $-\alpha$ (if $\alpha < 0$) can be computed by the following equation:

$$
{}_aD_t^{\alpha}x(t) = \lim_{h \to 0} \left[\frac{1}{h^{\alpha}} \sum_{k=0}^{\left[\frac{t-a}{h}\right]} (-1)^k \frac{\Gamma(\alpha+1)}{\Gamma(k+1)\Gamma(\alpha-k+1)} x(t-kh) \right] \tag{2}
$$

where h is the time increment, and Γ is the Gamma function. This function represents an extension of the factorial function to real and complex numbers. It is defined as follows:

$$\Gamma(z) = \int_0^\infty t^{z-1} e^{-t} dt \tag{3}$$

From a practical point of view, Eq. (2) is unusable since the number of addends tends towards infinity as h tends towards zero. Consequently, to obtain a computationally feasible discrete-time implementation, Eq. (2) is approximated by adopting a finite sampling time T_s [49]:

$$\begin{gathered} D_t^\alpha x(t) \cong D^\alpha x_k = \left[\frac{1}{{T_s}^\alpha} \sum_{j=0}^{k} w_j^\alpha x(t - jT_s)\right], \\ k = \left[\frac{t-a}{T_s}\right], \\ w_0^\alpha = 1, \\ w_j^\alpha = \left(1 - \frac{\alpha+1}{j}\right) w_{j-1}^\alpha \text{ for } j \geq 1. \end{gathered} \tag{4}$$

Even adopting the time-sampled approximation (4), the number of addends increases at each time step. Therefore, to obtain a discrete approximation suitable for implementation on a real-time digital controller, it is necessary to limit the number of considered previous steps to an adequate value, *n*. This corresponds to evaluating FO derivatives and integrals utilizing the digital filter of order *n* expressed by the following z-transfer function:

$$D^\alpha(z) = \left[\frac{1}{{T_s}^\alpha} \sum_{j=0}^{n} w_j^\alpha z^{-j}\right] \tag{5}$$

This filter has fixed memory length $L = nT_s$, while Eq. (2) considers all the time-history of *x(t)*. Nevertheless, since the coefficients w_j^α tend to zero as *j* tends to infinity, the oldest part of the history of *x(t)* can be neglected without significant approximations (*short-memory principle*, [2]).

3. The PII$^{1/2}$DD$^{1/2}$ control scheme

The well-known PID control law is based on the proportional, integral, and derivative gains K_p, K_i, and K_d. Using the differintegration operator defined in Section 2, the PID control law can be expressed in the following form:

$$u(e) = \left(K_p + K_i D^{-1} + K_d D^1\right) e \tag{6}$$

where u is the control action and e is the error, which is the difference between the reference set-point and the measured signal.

In the PII$^{1/2}$DD$^{1/2}$ scheme, two additional terms are introduced, the half-derivative term and the half-integral term:

$$u(e) = \left(K_p + K_i D^{-1} + K_{hi} D^{-1/2} + K_d D^1 + K_{hd} D^{1/2}\right) e \tag{7}$$

where K_{hd} and K_{hi} are respectively the *half-derivative gain* and the *half-integral gain*.

Applying the Laplace transform to Eqs. (6) and (7) with null initial conditions, we obtain the transfer functions $G_c(s) = U(s)/E(s)$ of the two controllers:

$$G_{c,PID}(s) = K_p + \frac{K_i}{s} + K_d s = K_i \frac{\left(1 + \left(K_p/K_i\right)s + \left(K_d/K_i\right)s^2\right)}{s} \tag{8}$$

$$\begin{aligned} G_{c,PII^{1/2}DD^{1/2}}(s) &= K_p + \frac{K_i}{s} + \frac{K_{hi}}{s^{1/2}} + K_d s + K_{hd} s^{1/2} = \\ &= K_i \frac{1 + \left(K_{hi}/K_i\right)s^{1/2} + \left(K_p/K_i\right)s + \left(K_{hd}/K_i\right)s^{3/2} + \left(K_d/K_i\right)s^2}{s} \end{aligned} \tag{9}$$

A FO system has commensurate-order *q* if all its orders of differintegration are integer multiples of *q*, with $q \in R^+$ [50]. Similarly to IO systems, the frequency response of FO systems can be evaluated by calculating the transfer function for $s = j\omega$, $\omega \in (0, \infty)$. Moreover, a system *G$_q$(s)* with commensurate-order *q* can be factored in the following form:

$$G_q(s) = k \frac{\prod_{i=0}^{m}\left(s^q - z_i\right)}{\prod_{j=0}^{n}\left(s^q - p_j\right)}, z_i \neq p_j \tag{10}$$

According to this factorization, is possible to obtain the Bode plot of *G$_q$(s)* by adding contributions of terms of order *q:* for each term $(s^q - r)^{\pm 1}$ with $r \neq 0$, the asymptotic magnitude plot has slope which varies from zero to $\pm q20$ dB/dec at the corner frequency $|r|^{1/q}$, while the asymptotic phase plot varies from 0 to $\pm q\pi/2$ at the same frequency $|r|^{1/q}$. Moreover, there is resonance for $q > 1$ [50].

IO systems are FO systems with unitary commensurate order; therefore, adopting the factorization (10), the PID transfer function (8) can be rewritten as follows:

$$G_{c,PID}(s) = K_d \frac{(s - z_1)(s - z_2)}{s} \tag{11}$$

where the zeros z_1 and z_2 are:

$$\begin{aligned} z_1 &= -\frac{K_p - \sqrt{K_p^2 - 4K_d K_i}}{2K_d} \\ z_2 &= -\frac{K_p + \sqrt{K_p^2 - 4K_d K_i}}{2K_d} \end{aligned} \tag{12}$$

If $K_p > 2(K_d K_i)^{1/2}$, z_1 and z_2 are real negative, and the asymptotic Bode plot is characterized by two corner frequencies, $\omega_{c1} = -z_1$ and $\omega_{c2} = -z_2$. For frequencies lower than $\omega_{c,1}$ the asymptotic magnitude slope is -20 dB/dec and the asymptotic phase is $-\pi/2$; between ω_{c1} and ω_{c2} the asymptotic magnitude slope and the asymptotic phase are null; for frequencies higher than ω_{c2} the asymptotic magnitude slope is $+20$ dB/dec and the asymptotic phase is $+\pi/2$.

The PII$^{1/2}$DD$^{1/2}$ controller is a commensurate-order system with order $q = 1/2$, therefore its transfer function (9), adopting the factorization (10), can be rewritten as follows:

$$G_{c,PII^{1/2}DD^{1/2}}(s) = \frac{K_i}{s} \prod_{i=1}^{4} \left(1 - \frac{s^{1/2}}{z'_i}\right) \tag{13}$$

According to Eq. (13), the asymptotic Bode plot can be drawn as follows: at low frequencies, the magnitude slope is -20 dB/dec, and the phase is $-\pi/2$ rad; after each corner frequency $\omega'_{c,i} = |z'_i|^2$, there is an increment of 10 dB/dec for the magnitude slope, and of $\pi/4$ rad for the phase. Consequently, after the fourth corner frequency, the magnitude slope is $+20$ dB/dec, and the phase is $+\pi/2$ rad.

Starting from factorization (13), in which K_i is present, the four remaining PII$^{1/2}$DD$^{1/2}$ gains can be calculated as a function of the *half-zeros* z'_i [44]:

$$K_p = K_i \left(\frac{1}{z'_1 z'_2} + \frac{1}{z'_1 z'_3} + \frac{1}{z'_1 z'_4} + \frac{1}{z'_2 z'_3} + \frac{1}{z'_2 z'_4} + \frac{1}{z'_3 z'_4}\right) \tag{14}$$

$$K_d = \frac{K_i}{z'_1 z'_2 z'_3 z'_4} \tag{15}$$

$$K_{hi} = K_i \left(-\frac{1}{z'_1} - \frac{1}{z'_2} - \frac{1}{z'_3} - \frac{1}{z'_4}\right) \tag{16}$$

$$K_{hd} = K_i \left(-\frac{1}{z'_1 z'_2 z'_3} - \frac{1}{z'_1 z'_2 z'_4} - \frac{1}{z'_1 z'_3 z'_4} - \frac{1}{z'_2 z'_3 z'_4}\right) \tag{17}$$

Employing Eqs. (14) to (17), it is possible to calculate the PII$^{1/2}$DD$^{1/2}$ gains starting from K_i and $\omega'_{c,i}$, $i = 1\ldots4$. In [44], a PII$^{1/2}$DD$^{1/2}$ tuning method is proposed, which starts from a given PID controller and derives the PII$^{1/2}$DD$^{1/2}$ gains by imposing the following conditions:

- the four corner frequencies of the PII$^{1/2}$DD$^{1/2}$ controller are symmetrically placed in logarithmic scale, that is:

$$\frac{\omega'_{c,2}}{\omega'_{c,1}} = \frac{\omega'_{c,4}}{\omega'_{c,3}} \tag{18}$$

- the initial and final asymptotes of the PID and PII$^{1/2}$DD$^{1/2}$ controllers, with slopes of −20 dB/dec and +20 dB/dec, are coincident;
- the magnitude of the central zone with null slope is the same for the PID and PII$^{1/2}$DD$^{1/2}$.

Fig. 1 shows the asymptotic Bode plots of one PID and one PII$^{1/2}$DD$^{1/2}$ controller fulfilling these conditions, which are verified if [44]:

- the integral gains of the PID and PII$^{1/2}$DD$^{1/2}$ controllers, which define the first asymptote, are equal;
- the following ratios between the corner frequencies of the PID and PII$^{1/2}$DD$^{1/2}$ controllers hold:

$$\omega'_{c1} = \frac{\omega_{c1}}{\rho}; \omega'_{c2} = \rho\omega_{c1}; \omega'_{c3} = \frac{\omega_{c2}}{\rho}; \omega'_{c4} = \rho\omega_{c2} \tag{19}$$

with $1 < \rho < \rho_{\max} = (\omega_{c2}/\omega_{c1})^{1/2}$.

Condition (19) means that $\omega'_{c,1}$ and $\omega'_{c,2}$ have the same distance from $\omega_{c,1}$ in logarithmic scale, and that there is the same distance between $\omega'_{c,3}$ and $\omega_{c,2}$, and between $\omega_{c,2}$ and $\omega'_{c,4}$. If $\rho = \rho_{\max}$ the corner frequencies ω'_{c2} and ω'_{c3} coincide. If $\rho = 1$ the asymptotic Bode plots of PID and PII$^{1/2}$DD$^{1/2}$ are equal ($\omega'_{c1} = \omega'_{c2} = \omega_{c1}$, and $\omega'_{c3} = \omega'_{c4} = \omega_{c2}$); nevertheless, the exact Bode plots of the two controllers are different [44].

Adopting this tuning method, the PII$^{1/2}$DD$^{1/2}$ controller is fully determined from a given PID controller once the ratio ρ is selected. The possible benefits of this approach have been analysed in simulation and experimentally for the position control of a mechatronic axis [44]. The comparison between the PID and PII$^{1/2}$DD$^{1/2}$ controllers is generalized adopting a nondimensional formulation in the next section.

4. Nondimensional formulation of the PID and PII$^{1/2}$DD$^{1/2}$ position control of a purely inertial system

Let us consider a purely inertial second-order plant (double integrator, Fig. 2). In the following, a rotor will be considered, with angular position θ, inertia J, and driven by a control torque M. Nevertheless, this model can also be used to represent a translational system (a mass m driven by a control force F).

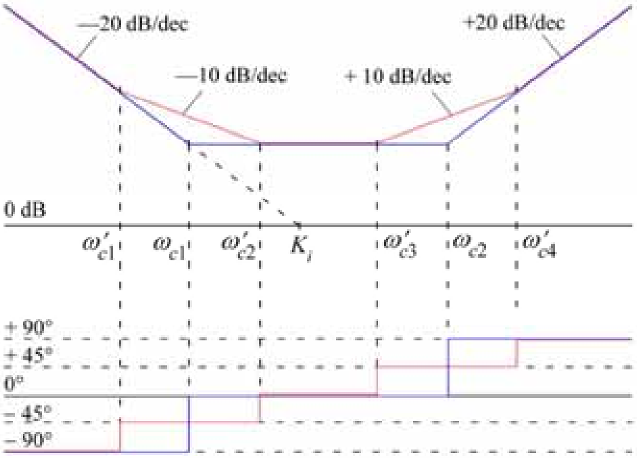

Fig. 1. Comparison of PID and PII$^{1/2}$DD$^{1/2}$ asymptotic Bode plots.

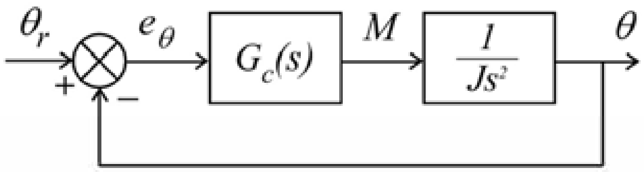

Fig. 2. Closed-loop control of a purely inertial system.

The dynamics of the rotor, in the absence of friction, is expressed by the following second-order linear equation, without first-order and zero-order terms:

$$J\frac{d^2}{dt^2}\theta = M(e_\theta) \tag{20}$$

The controller calculates the torque M as a function of e_θ, which is the difference (error) between the set-point angle θ_r and the measured angle θ. The control output is calculated using law (6) in the case of PID control or law (7) in the case of PII$^{1/2}$DD$^{1/2}$ control. For the sake of generality, the two controllers are compared through a dimensionless approach. To this aim, it is necessary to introduce the *dimensionless time* t_{ad}, the *dimensionless angle* θ_{ad}, and the *dimensionless error* e_{ad}:

$$t_{ad} = \omega_n t \tag{21}$$

$$\theta_{ad} = \theta / \theta_r \tag{22}$$

$$e_{\theta,ad} = e_\theta / \theta_r \tag{23}$$

where:

$$\omega_n = \sqrt{K_p/J} \tag{24}$$

Let us introduce the operatorD^α_{ad}, which is the same operator defined in Eq. (1) but applied to a function of the dimensionless time t_{ad}. From Eqs. (1) and (21), it follows that:

$$D^\alpha = \omega_n^\alpha D^\alpha_{ad} \tag{25}$$

Using Eqs. (6) and (20)–(25), the following dynamic model of the PID closed-loop system can be obtained:

$$D^2_{ad}\theta_{ad} = e_{\theta,ad} + \delta D^{-1}_{ad} e_{\theta,ad} + 2\zeta D^1_{ad} e_{\theta,ad} \tag{26}$$

where the dimensionless parameters δ and ζ represent nondimensionally the gains K_i and K_d:

$$\delta = \frac{K_i}{K_p\omega_n} = \frac{K_i J^{1/2}}{K_p^{3/2}} \tag{27}$$

$$\zeta = \frac{K_d}{2K_p}\omega_n = \frac{K_d}{2\sqrt{K_p J}} \tag{28}$$

Similarly, using Eqs. (7) and (20)–(25), the dynamic model of the PII$^{1/2}$DD$^{1/2}$ closed-loop system can be obtained:

$$\begin{aligned} D^2_{ad}\theta_{ad} &= e_{\theta,ad} + \delta D^{-1}_{ad} e_{\theta,ad} + \gamma D^{-1/2}_{ad} e_{\theta,ad} + \\ &+ 2\zeta D^1_{ad} e_{\theta,ad} + \psi D^{1/2}_{ad} e_{\theta,ad} \end{aligned} \tag{29}$$

where two further dimensionless parameters γ and ψ represent nondimensionally the gains K_{hi} and K_{hd}:

$$\gamma = \frac{K_{hi}}{K_p\omega_n^{1/2}} = \frac{K_{hi} J^{1/4}}{K_p^{5/4}} \tag{30}$$

$$\psi = \frac{K_{hd}}{K_p}\omega_n^{1/2} = \frac{K_{hd}}{K_p^{3/4} J^{1/4}} \tag{31}$$

Equations (21–31) lead to the dimensionless scheme of Fig. 3, where

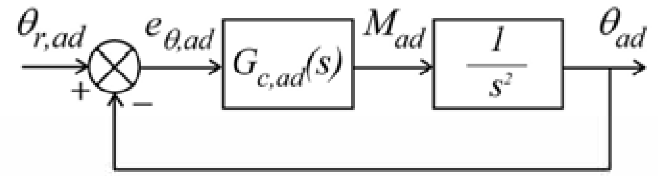

Fig. 3. Dimensionless model of the closed-loop control of a purely inertial system.

$M_{ad} = M / K_p$ is the dimensionless control torque.

In the scheme of Fig. 3, the dimensionless transfer function $G_{c,ad}(s)$ has the following expressions in the PID and PII$^{1/2}$DD$^{1/2}$ cases:

$$G_{c,ad,PID}(s) = 1 + \frac{\delta}{s} + 2\zeta s =$$

$$= \frac{\delta}{s}\left(1 + \frac{s}{\delta} + \frac{2\zeta}{\delta}s^2\right) = \frac{\delta}{s}\left(1 - \frac{s}{z_{1,ad}}\right)\left(1 - \frac{s}{z_{2,ad}}\right) \tag{32}$$

$$G_{c,ad,PII^{1/2}DD^{1/2}}(s) = 1 + \psi s^{1/2} + 2\zeta s + \frac{\gamma}{s^{1/2}} + \frac{\delta}{s} =$$

$$= \frac{\delta}{s}\left(1 + \frac{\gamma}{\delta}s^{1/2} + \frac{s}{\delta} + \frac{\psi}{\delta}s^{3/2} + \frac{2\zeta}{\delta}s^2\right) = \frac{\delta}{s}\prod_{i=1}^{4}\left(1 - \frac{s^{1/2}}{z_{i,ad}}\right) \tag{33}$$

Starting from Eqs. (32) and (33), it is possible to obtain the dimensionless closed-loop transfer functions for the two control laws:

$$G_{cl,ad,PID}(s) = \frac{\theta_{ad}(s)}{\theta_{r,ad}(s)} = \frac{1 + \delta s^{-1} + 2\zeta s}{1 + \delta s^{-1} + 2\zeta s + s^2} \tag{34}$$

$$\begin{aligned} G_{cl,ad,PII^{1/2}DD^{1/2}}(s) &= \frac{\theta_{ad}(s)}{\theta_{r,ad}(s)} = \\ &= \frac{1 + \delta s^{-1} + \gamma s^{-1/2} + 2\zeta s + \psi s^{3/2}}{1 + \delta s^{-1} + \gamma s^{-1/2} + 2\zeta s + \psi s^{3/2} + s^2} \end{aligned} \tag{35}$$

To apply the tuning method proposed in Section 3 to the dimensionless model, also the corner frequencies of the PID controller, Eq. (12), can be nondimensionalized as follows:

$$\begin{aligned} \omega_{c1,ad} &= \frac{\omega_{c1}}{\omega_n} = -z_{1,ad} = \frac{1 - \sqrt{1 - 8\delta\zeta}}{4\zeta} \\ \omega_{c2,ad} &= \frac{\omega_{c2}}{\omega_n} = -z_{2,ad} = \frac{1 + \sqrt{1 - 8\delta\zeta}}{4\zeta} \end{aligned} \tag{36}$$

Once the ratio ρ is selected, the four dimensionless PII$^{1/2}$DD$^{1/2}$ corner frequencies can be obtained:

$$\begin{aligned} \omega'_{c1,ad} &= \frac{\omega_{c1,ad}}{\rho}; \omega'_{c2,ad} = \rho\omega_{c1,ad}; \\ \omega'_{c3,ad} &= \frac{\omega_{c2,ad}}{\rho}; \omega'_{c4,ad} = \rho\omega_{c2,ad} \end{aligned} \tag{37}$$

Then, considering the relationship between the half zeros and the corner frequencies $z_i = -(\omega'_{c,i})^{1/2}$, $i = 1 \,..\, 4$ [44], it is possible to calculate the *dimensionless half-zeros* $z'_{i,ad}$:

$$z'_{i,ad} = -\left(\omega'_{ci,ad}\right)^{1/2}, i = 1...4 \tag{38}$$

Finally, the dimensionless version of Eqs. (14) to (17) can be derived:

$$\begin{aligned} \frac{1}{\delta} = \Bigg(&\frac{1}{z'_{1,ad}z'_{2,ad}} + \frac{1}{z'_{1,ad}z'_{3,ad}} + \frac{1}{z'_{1,ad}z'_{4,ad}} + \\ &+ \frac{1}{z'_{2,ad}z'_{3,ad}} + \frac{1}{z'_{2,ad}z'_{4,ad}} + \frac{1}{z'_{3,ad}z'_{4,ad}}\Bigg) \end{aligned} \tag{39}$$

$$\frac{2\zeta}{\delta} = \frac{1}{z'_{1,ad}z'_{2,ad}z'_{3,ad}z'_{4,ad}} \tag{40}$$

$$\frac{\gamma}{\delta} = \left(-\frac{1}{z'_{1,ad}} - \frac{1}{z'_{2,ad}} - \frac{1}{z'_{3,ad}} - \frac{1}{z'_{4,ad}}\right) \tag{41}$$

$$\begin{aligned} \frac{\psi}{\delta} = \Bigg(&-\frac{1}{z'_{1,ad}z'_{2,ad}z'_{3,ad}} - \frac{1}{z'_{1,ad}z'_{2,ad}z'_{4,ad}} + \\ &- \frac{1}{z'_{1,ad}z'_{3,ad}z'_{4,ad}} - \frac{1}{z'_{2,ad}z'_{3,ad}z'_{4,ad}}\Bigg) \end{aligned} \tag{42}$$

5. Comparison of the closed-loop step response of the PID and PII$^{1/2}$DD$^{1/2}$ controllers

The step responses of the dimensionless PID and PII$^{1/2}$DD$^{1/2}$ closed-loop systems defined by Eqs. (34) and (35) have been compared in simulation employing the FOTM MatLab toolbox [49].

The 3D graphs in Figs. 4, 5, 6, and 7 represent, respectively, the dimensionless settling time to within 2 % ($T_{s,ad}$), the dimensionless rise time from 10 % to 90 % of the final value ($T_{r,ad}$), the percent overshoot (%OS), and the phase margin (PM) obtained using the two controllers, as functions of ζ and δ. Using the dimensionless formulation, the closed-loop system with the PID controller is fully defined by these two parameters, as shown by Eq. (34). On the contrary, the closed-loop system with the PII$^{1/2}$DD$^{1/2}$ controller tuned with the method discussed in Section 4 (Eqs. (37)-(42)) is defined once selected the parameter ρ, besides ζ and δ. Therefore, while in the 3D graphs of Fig. 4-7 there is only one surface for the PID (green), for the PII$^{1/2}$DD$^{1/2}$ controller there are different surfaces, obtained for 9 values of ρ in geometric progression from $2^0 = 1$ to $2^4 = 16$, represented with a colour scale ranging from blue to red.

On the left 3D graphs of Figs. 4-7, ζ varies from 0 to 2, and δ varies from 0 to 0.1. Note that in these graphs there is a zone of the $\zeta-\delta$ space in which the PII$^{1/2}$DD$^{1/2}$ surfaces are not calculated. In this zone, coloured in yellow in the base $\zeta-\delta$ plane, the tuning method proposed in Section 4 cannot be applied since the two zeros of the PID controller are not real but conjugate complex. Considering Eq. (36), it is clear that, to apply the proposed PII$^{1/2}$DD$^{1/2}$ tuning method, it is necessary to have a PID with two real negative zeros, which corresponds to the following condition:

$$\delta\zeta \leq \frac{1}{8} \tag{43}$$

Condition (43) is not fulfilled in the zone of the ζ-δ plane represented in yellow in the left graphs of Fig. 4-7, delimited by the hyperbole $8\zeta = 1/\delta$.

The level curves of the 3D graphs in Fig. 4-6, related to time-domain performance parameters, can be used to compare the behaviour of the PID and PII$^{1/2}$DD$^{1/2}$ controllers with equal settling time, rise time, or overshoot. The left plots of Figs. 8-10 represent the level curves of the 3D surfaces of Figs. 4-6, respectively, at $T_{s,ad} = 5$, $T_{r,ad} = 0.5$, and 30 % overshoot. Once the level curves at the desired level are obtained, it is necessary to impose another condition to define the comparison. A possible choice is to select the amount of integral action in terms of δ. For example, the horizontal dashed lines in the left plots of Figs. 8-10 impose the condition $\delta = 0.01$, defining one PID tuning and a PII$^{1/2}$DD$^{1/2}$ tuning for each value of ρ. Then, the step responses corresponding to these tunings are compared in the right plots of Figs. 8-10. It is possible to draw the following conclusions:

- for all three comparisons, the influence of ρ is not remarkable, and the differences among the PII$^{1/2}$DD$^{1/2}$ tunings are much lower than the difference with respect to the PID;
- in the comparison with equal dimensionless settling time $T_{s,ad} = 5$ (Fig. 8), the PII$^{1/2}$DD$^{1/2}$ exhibits lower dimensionless rise time (0.61÷0.66 depending on ρ, vs. 0.81 of the PID); on the other hand, the PID has lower overshoot (18.8 %) with respect to the PII$^{1/2}$DD$^{1/2}$ (36.7 %÷38.3 % depending on ρ);

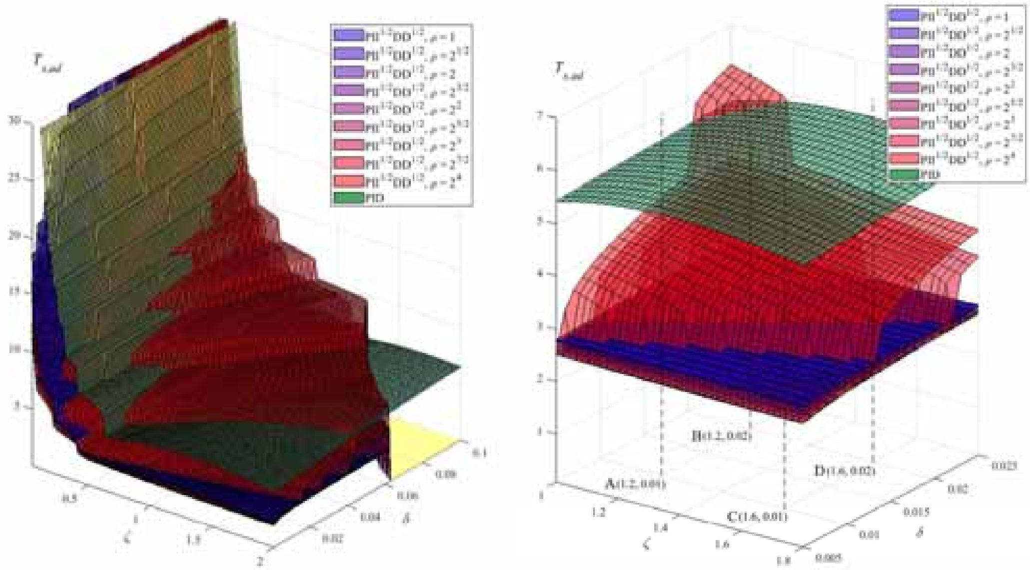

Fig. 4. Step response of the closed-loop system with PID and PII$^{1/2}$DD$^{1/2}$ controllers: settling time to within 2% as a function of ζ and δ. The graph on the right shows the detail of the region with $1 < \zeta < 1.8$ and $0.005 < \delta < 0.025$.

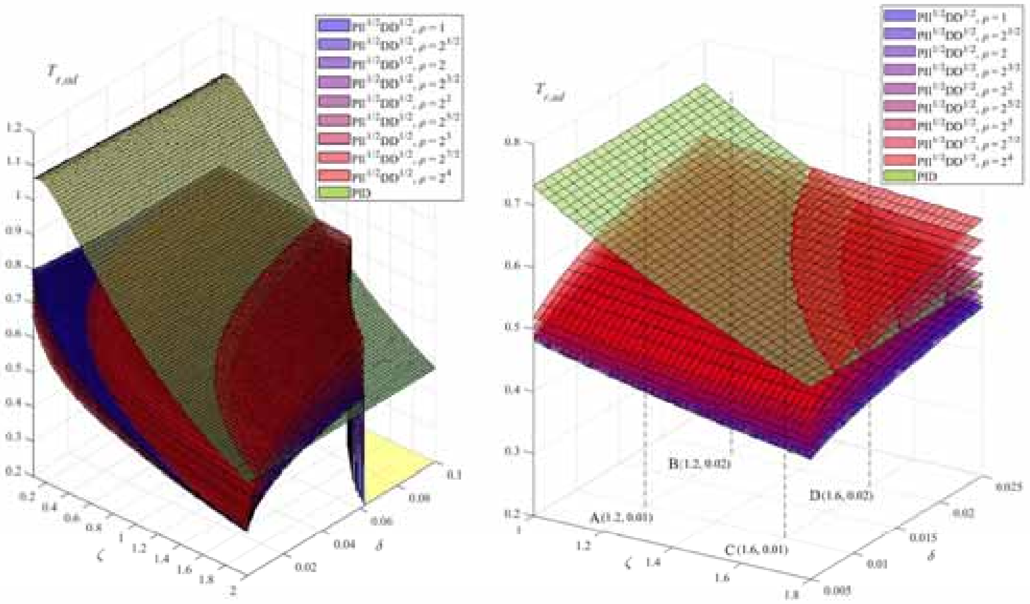

Fig. 5. Step response of the closed-loop system with PID and PII$^{1/2}$DD$^{1/2}$ controllers: rise time as a function of ζ and δ. The graph on the right shows the detail of the region with $1 < \zeta < 1.8$ and $0.005 < \delta < 0.025$.

- in the comparison with equal dimensionless rise time $T_{r,ad} = 0.5$ (Fig. 9), the PII$^{1/2}$DD$^{1/2}$ exhibits lower dimensionless settling time (2.60÷2.83 depending on ρ, vs. 5.46 of the PID); on the other hand, the PID has lower overshoot (5.5 %) with respect to the PII$^{1/2}$DD$^{1/2}$ (21.4 %÷24.4 % depending on ρ);
- in the comparison with equal overshoot (30 %, Fig. 10), the PII$^{1/2}$DD$^{1/2}$ obtains lower dimensionless rise time (0.55÷0.59 depending on ρ, vs. 0.94 of the PID) and also lower dimensionless settling time (3.57÷3.96 depending on ρ, vs. 7.5 of the PID).

In general, each performance comparison can be performed through the analysis of the level curves and depends on the considered level. To this aim, the .FIG files of the 3D surfaces represented in Figs. 4-7 are made available to make any specific comparison possible (see supplementary materials).

It is possible to note that the adoption of the FO controller improves the system readiness in the zone with higher ζ and lower δ, which is represented in detail in the right graphs of Figs. 4-7, with $1 < \zeta < 1.8$ and $0.005 < \delta < 0.025$. As a matter of fact, in this zone, the settling time of the PII$^{1/2}$DD$^{1/2}$ controller is lower for any value of ρ, except for a limited zone close to the corner with $\zeta = 1$ and $\delta = 0.025$, and only for the maximum value of ρ (Fig. 4, right). Also, the rise time is in general lower for the FO controller (Fig. 5, right), even if in the zone close to the corner with $\zeta = 1.8$ and $\delta = 0.025$ the PID has lower rise time than the PII$^{1/2}$DD$^{1/2}$ with the higher values of ρ. On the other hand, the drawback of the FO controller is the overshoot, which is higher for any combination of ζ, δ, and ρ in the zone with $1 < \zeta < 1.8$ and $0.005 < \delta < 0.025$ (Fig. 6, right). Coherently, in this zone, the phase margin is higher for the IO controller (Fig. 7, right). On the other hand, in the case of low values of ζ, the stability is better for the FO controller, with lower overshoot (Fig. 6, left) and higher phase margin (Fig. 7, left).

The vertical dashed lines of the right graphs of Fig. 4-7 correspond to

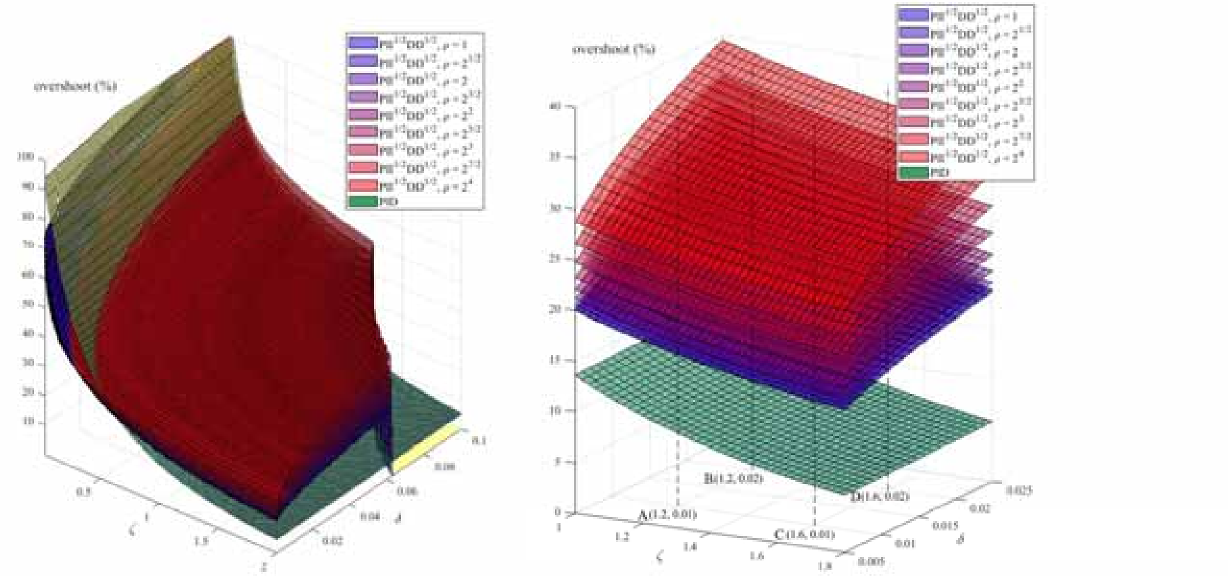

Fig. 6. Step response of the closed-loop system with PID and $PII^{1/2}DD^{1/2}$ controllers: overshoot as a function of ζ and δ. The graph on the right shows the detail of the region with $1 < \zeta < 1.8$ and $0.005 < \delta < 0.025$.

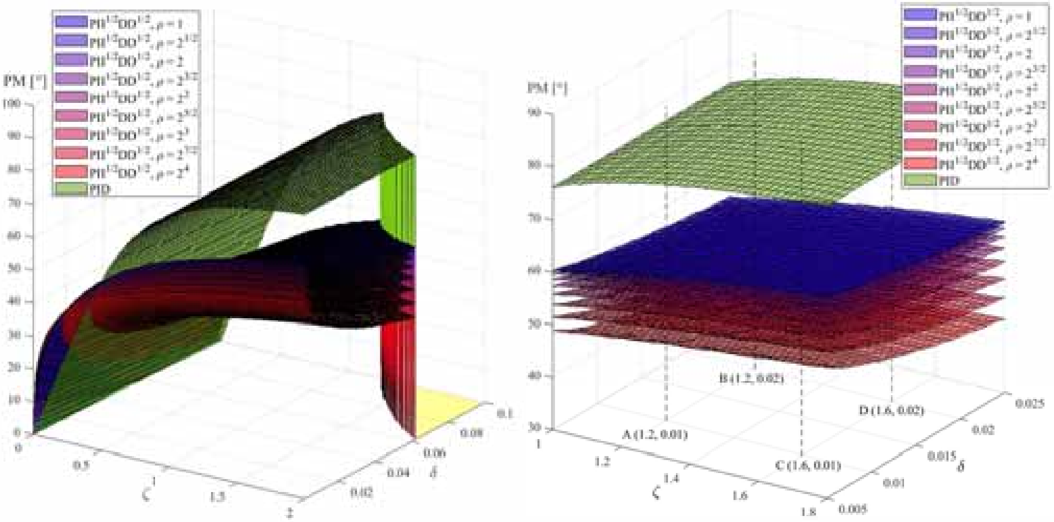

Fig. 7. Phase margins of the system with PID and $PII^{1/2}DD^{1/2}$ controllers as functions of ζ and δ. The graph on the right shows the detail of the region with $1 < \zeta < 1.8$ and $0.005 < \delta < 0.025$.

four ζ-δ combinations (A, B, C, and D), with $\zeta = 1.2$ or 1.6, and with $\delta = 0.01$ or 0.02, representative of the behaviour of the two systems in the zone of the ζ-δ space with $1 < \zeta < 1.8$ and $0.005 < \delta < 0.025$.

Figure 11 shows the time histories of θ_{ad} for the PID and $PII^{1/2}DD^{1/2}$ controllers corresponding to these four ζ-δ combinations. Since the $PII^{1/2}DD^{1/2}$ tuning depends on ρ, three values have been considered for this parameter, in geometric progression: 1, $\rho_{\max}^{1/2}$ and $\rho_{\max}$. Considering Eq. (36), it is possible to calculate $\rho_{\max}$ as a function of ζ and δ:

$$\rho_{\max} = \sqrt{\frac{\omega_{c2,ad}}{\omega_{c1,ad}}} = \sqrt{\frac{1+\sqrt{1-8\delta\zeta}}{1-\sqrt{1-8\delta\zeta}}} \tag{44}$$

Fig. 12 represents the comparison in the frequency domain of the PID and $PII^{1/2}DD^{1/2}$ controllers for the same ζ-δ combinations and for the same values of ρ considered in Figure 11, showing the Bode plots of the closed-loop transfer functions (34) and (35). Table 1 collects the dimensionless control parameters, the dimensionless settling time, the dimensionless rise time, the percent overshoot, and the phase margin of the two controllers for the A, B, C, and D ζ-δ combinations.

The observation of Figs. 11 and 12 and Table 1 confirms that in the zone of the ζ-δ plane with $\zeta > 1$ and $\delta < 0.025$ the FO controller has better readiness than the IO controller, in terms of lower settling time, lower rise time, and larger closed-loop bandwidth. On the other hand, the $PII^{1/2}DD^{1/2}$ scheme has the drawback of worse stability, shown by a larger overshoot and lower phase margin. These features are amplified by higher values of ρ.

6. Application to a real mechatronic axis

The results obtained with the nondimensional approach in Section 5 are related to a step set-point, which is unsuitable for application to position control of a real mechatronic axis due to the actuation peaks it produces. Hence, position control is always performed using smoother motion profiles. Nevertheless, the step response analysis is widely used to characterize linear systems, comparing the readiness, accuracy, and stability of different controllers.

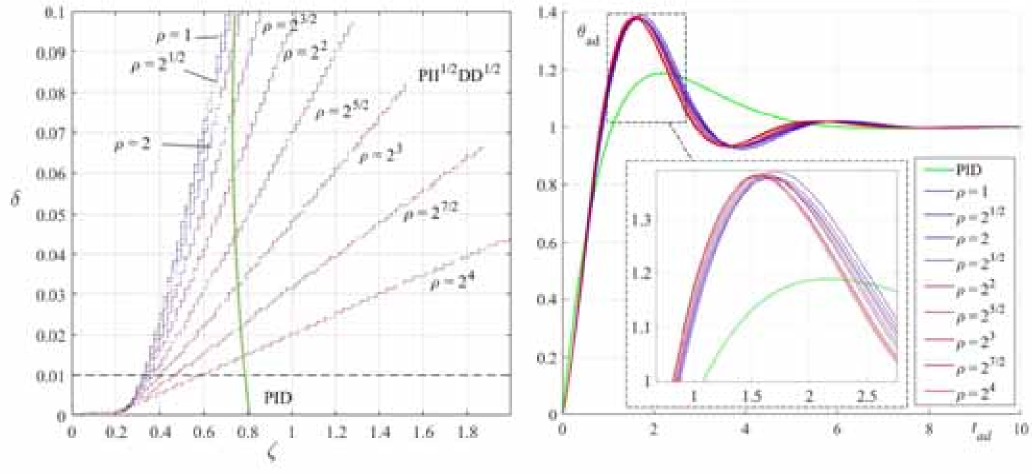

Fig. 8. Step response of the closed-loop system with PID and PII$^{1/2}$DD$^{1/2}$ controllers, with settling time $T_{s,ad} = 5$ and $\delta = 0.01$. Left: level curves of the 3D surfaces of Fig. 4 at $T_{s,ad} = 5$. Right: step responses of the systems corresponding to the intersections of the level curves with the dashed straight line at $\delta = 0.01$.

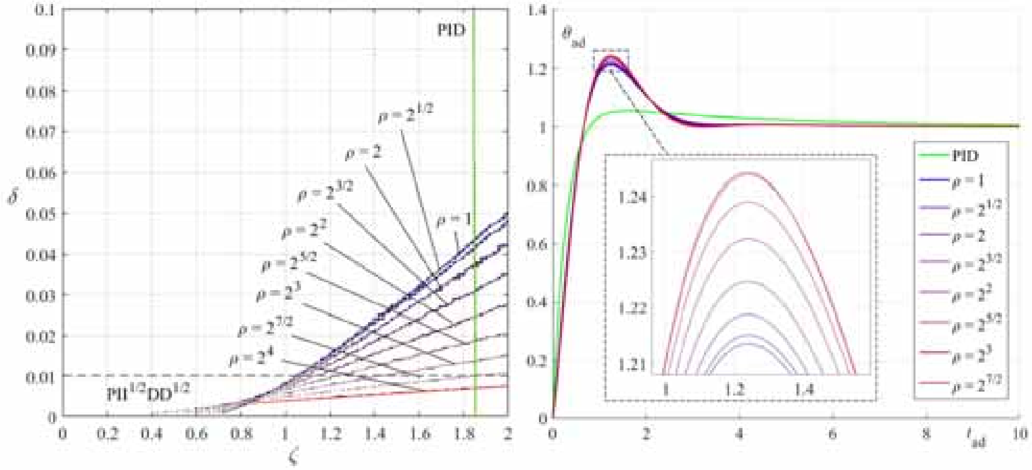

Fig. 9. Step response of the closed-loop system with PID and PII$^{1/2}$DD$^{1/2}$ controllers, with settling time $T_{r,ad} = 0.5$ and $\delta = 0.01$. Left: level curves of the 3D surfaces of Fig. 5 at $T_{r,ad} = 0.5$. Right: step responses of the systems corresponding to the intersections of the level curves with the dashed straight line at $\delta = 0.01$.

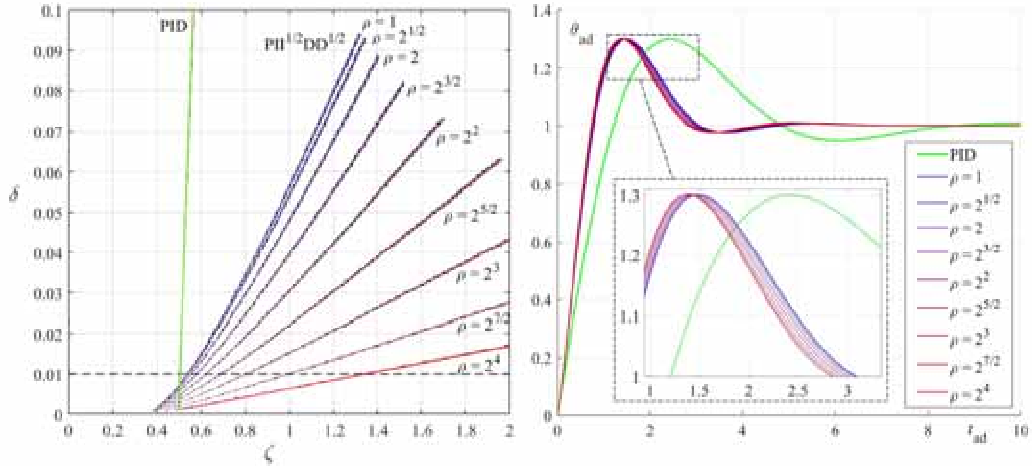

Fig. 10. Step response of the closed-loop system with PID and PII$^{1/2}$DD$^{1/2}$ controllers, with 30% overshoot and $\delta = 0.01$. Left: level curves of the 3D surfaces of Fig. 6 at 30% overshoot. Right: step responses of the systems corresponding to the intersections of the level curves with the dashed straight line at $\delta = 0.01$.

The comparison of the PID and PII$^{1/2}$DD$^{1/2}$ control schemes is carried out in Section 5 using a nondimensional model and considering a unit step input for the sake of generality. It is possible to perform a nondimensional comparison also with different set-point profiles, but it leads to the following problems:

- the comparison depends on the type of motion profile (trapezoidal speed law, cycloidal, polynomial, etc.);
- even if a single profile type is considered, it is necessary to introduce further nondimensional parameters; for example, for the trapezoidal speed law, it is necessary to consider the ratio between the motion

Table 1

Dimensionless control parameters (ζ, δ, ρ), dimensionless settling time ($T_{s,ad}$) and rise time ($T_{s,ad}$), percent overshoot (%OS), and phase margin (PM) of the PID and $\mathrm{PII}^{1/2}\mathrm{DD}^{1/2}$ controllers for the four ζ-δ combinations A, B, C, and D of Figs. 4-7.

$\zeta-\delta$ combination, controller		ζ	δ	ρ	$T_{s,ad}$	$T_{r,ad}$	%OS	PM
A	PID	1.2	0.01	–	5.71	0,6618	10.65 %	80°
	$\mathrm{PII}^{1/2}\mathrm{DD}^{1/2}$, $\rho = 1$	1.2	0.01	1	2.83	0,4807	19.82 %	61°
	$\mathrm{PII}^{1/2}\mathrm{DD}^{1/2}$, $\rho = (\rho_{\max})^{1/2}$	1.2	0.01	2.5092	2.75	0,4850	20.98 %	59°
	$\mathrm{PII}^{1/2}\mathrm{DD}^{1/2}$, $\rho = \rho_{\max}$	1.2	0.01	6.2961	2.65	0,5063	24.63 %	55°
B	PID	1.2	0.02	–	5.80	0,6614	10.79 %	80°
	$\mathrm{PII}^{1/2}\mathrm{DD}^{1/2}$, $\rho = 1$	1.2	0.02	1	2.87	0,5116	22.27 %	58°
	$\mathrm{PII}^{1/2}\mathrm{DD}^{1/2}$, $\rho = (\rho_{\max})^{1/2}$	1.2	0.02	2.0817	2.83	0,5167	23.19 %	57°
	$\mathrm{PII}^{1/2}\mathrm{DD}^{1/2}$, $\rho = \rho_{\max}$	1.2	0.02	4.3336	2.77	0,5356	26.02 %	53°
C	PID	1.6	0.01	–	5.71	0,5537	6.92 %	84°
	$\mathrm{PII}^{1/2}\mathrm{DD}^{1/2}$, $\rho = 1$	1.6	0.01	1	2.87	0,4391	16.79 %	65°
	$\mathrm{PII}^{1/2}\mathrm{DD}^{1/2}$, $\rho = (\rho_{\max})^{1/2}$	1.6	0.01	2.3249	2.79	0,4454	17.80 %	63°
	$\mathrm{PII}^{1/2}\mathrm{DD}^{1/2}$, $\rho = \rho_{\max}$	1.6	0.01	5.4052	2.64	0,4695	20.97 %	59°
D	PID	1.6	0.02	–	5.85	0,5535	7.00 %	84°
	$\mathrm{PII}^{1/2}\mathrm{DD}^{1/2}$, $\rho = 1$	1.6	0.02	1	2.90	0,4732	19.07 %	62°
	$\mathrm{PII}^{1/2}\mathrm{DD}^{1/2}$, $\rho = (\rho_{\max})^{1/2}$	1.6	0.02	1.9186	2.86	0,4789	19.82 %	61°
	$\mathrm{PII}^{1/2}\mathrm{DD}^{1/2}$, $\rho = \rho_{\max}$	1.6	0.02	3.6812	2.78	0,4979	22.11 %	58°

profile duration and the system natural period $2\pi/\omega_n$, and two ratios defining the durations of the three phases (acceleration, constant speed, deceleration); consequently, the number of possible 3D surfaces for the PID-$\mathrm{PII}^{1/2}\mathrm{DD}^{1/2}$ comparison is infinite since they depend on these ratios.

For these reasons, we have decided to perform a general comparison by adopting a nondimensional model and considering a unit step input; then, we have validated the tuning approach by simulation and experimentally on a real mechatronic axis in the case of trapezoidal speed law, which is the most commonly used in industry.

Moreover, in Section 5 simulations are related to continuous time systems, without taking into account the effects of the discrete-time implementation, with the approximation introduced by the finite-order digital filter (5) and by the limitations on the sampling time. On the contrary, in this section, the PID and $\mathrm{PII}^{1/2}\mathrm{DD}^{1/2}$ controllers will be compared in simulation and experimental tests in a real position control application under the following conditions:

- the control algorithms are implemented in discrete-time by using the digital filter (5), with sampling time T_s and finite memory length n limited by the computing capabilities of the controller;
- the position set-point is characterized by trapezoidal velocity profile in three phases: constant acceleration, constant velocity, and constant deceleration.

In particular, the experimental set-up is composed of:

- a controller (red subsystem in Fig. 13) implemented in Simulink Desktop Real-Time running on a PC equipped with a National Instrument PCI-6259 DAQ card; this controller realizes the position loop and provides the torque set-point to the driver; its

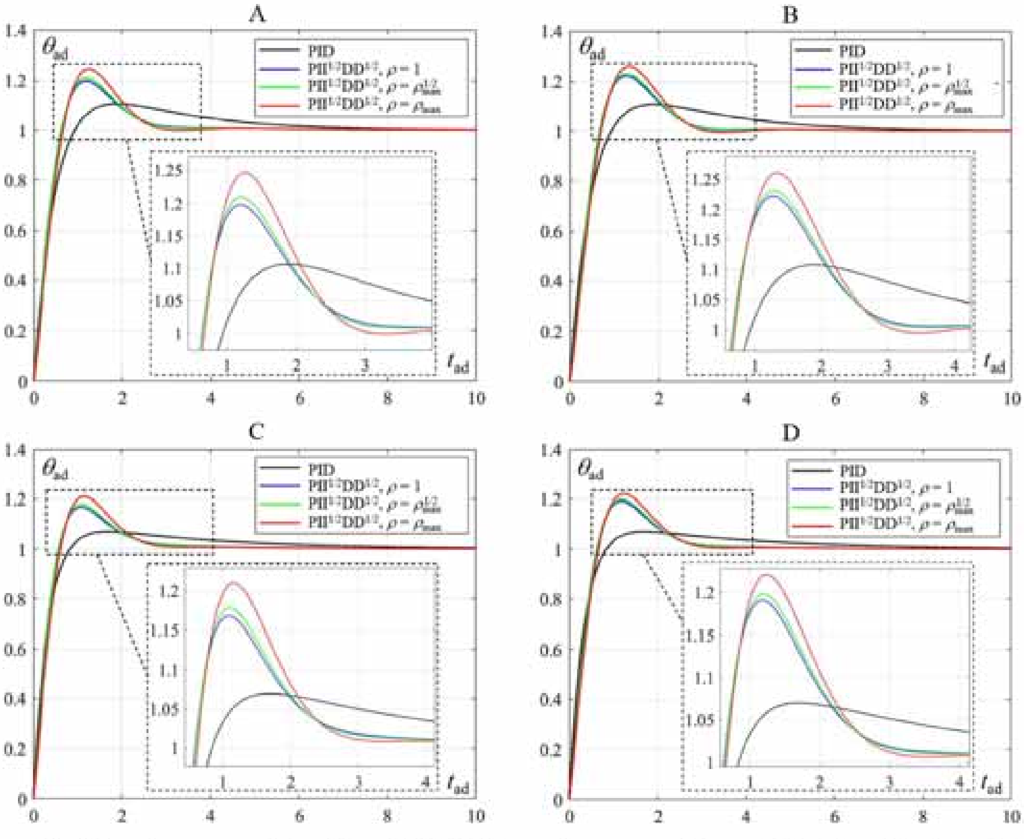

Fig. 11. Step responses of the closed-loop system with the PID and $\mathrm{PII}^{1/2}\mathrm{DD}^{1/2}$ controllers corresponding to the four ζ-δ combinations A, B, C, and D of Figs. 4-7.

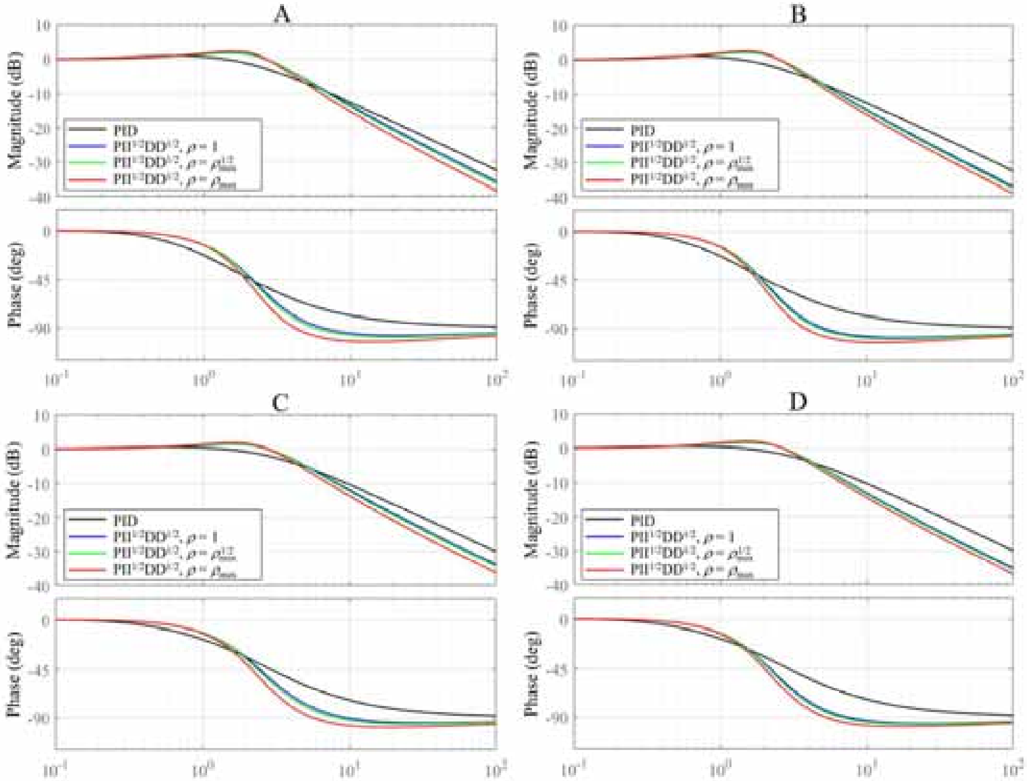

Fig. 12. Bode plots of the closed-loop frequency responses with the PID and $\mathrm{PII}^{1/2}\mathrm{DD}^{1/2}$ controllers corresponding to the four ζ-δ combinations A, B, C, and D of Figs. 4-7.

computational power is sufficient to calculate the FO terms employing the digital filter (5) with $T_s = 0.006$ s and $n = 6$;

- a Kollmorgen AKD-P00606 driver (magenta subsystem in Fig. 13), controlled in torque;
- the mechanical subsystem (orange in Fig. 13), composed of an inertial load (flywheel) directly connected to a brushless DC motor Kollmorgen AKM42G; the maximum continuous torque of the motor is 3.4 Nm, and the overall moment of inertia of the flywheel, shaft, joint, and motor rotor is $J = 1.047 \times 10^{-3}$ kgm^2.

The torque reference M_r is calculated by the position control with transfer function $G_c(s)$ (blue block in Fig. 13) using Eq. (6) for the PID or Eq. (7) for the $\mathrm{PII}^{1/2}\mathrm{DD}^{1/2}$. A feed-forward friction compensation is added to M_r to obtain the final torque set-point from the controller to the driver. The system considered in Sections 4 and 5, defined by Eq. (20), is a pure inertia without friction. Since friction of bearings is low but not negligible, the no-load torque of the experimental setup has been measured, obtaining that friction can be adequately approximated by a linear model with viscous coefficient $B = 1.80 \times 10^{-3}$ Nms/rad. Consequently, to reduce the difference between the frictionless model of Eq. (20) and the real system, a feed-forward compensation is added, proportional to the rotor velocity. The velocity is obtained by first-order derivation of the encoder signal through the coefficient $k_{ff} = B$ (Fig. 13). The green block of Fig. 13, with transfer function $G_p(s)$, represents the friction-compensated system, corresponding to the frictionless model (20).

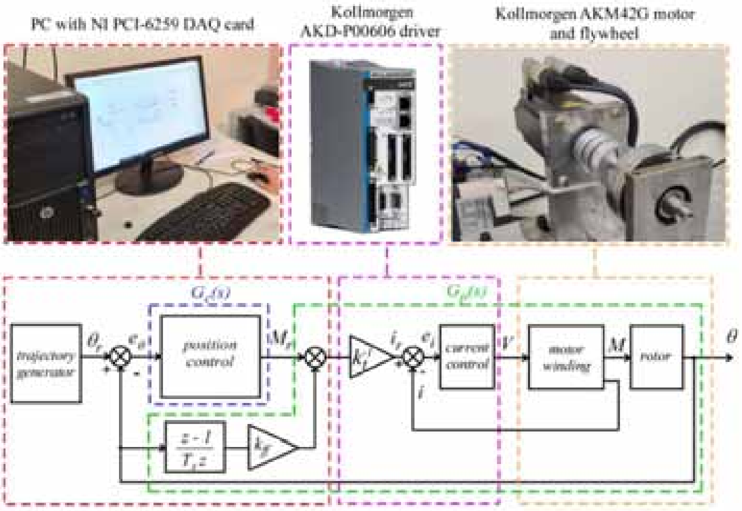

Fig. 13. Control layout of the experimental test bench.

Inside the driver, the current loop imposes the current reference i_r, obtained by dividing the torque reference by the motor torque constant $k_t = 0.7691$ Nm/A.

Since the controller is implemented in Simulink Desktop Real-Time, it has been applied both to the real system and to a virtual frictionless model. The real system differs from the model since its non-linear friction isn't exactly compensated by the linear feed-forward compensation; however, simulation and experimental results are in good agreement, as will be discussed in the following. The quantization error due to the digital encoder is negligible (2.4×10^{-5} rad).

The comparison between the PID and $\mathrm{PII}^{1/2}\mathrm{DD}^{1/2}$ controllers has been carried out with the following tuning criteria:

- the proportional gain of the PID controller is imposed: $K_p = 0.25$ Nm/rad; consequently, the natural frequency $\omega_n = 15.45$ rad/s has been calculated by means of Eq. (24);
- the four ζ-δ combinations of Table 1 (A, B, C, D) have been considered;
- since ω_n is known, the PID gains K_i and K_d have been obtained by Eqs. (27) and (28) for each ζ-δ combination;
- for the $\mathrm{PII}^{1/2}\mathrm{DD}^{1/2}$ controller, three values of ρ have been considered for each ζ-δ combination: 1, $\rho_{\max}^{1/2}$, and $\rho_{\max}$, as in Table 1; then, for any ζ-δ-ρ combination, the K_p, K_i, K_{hi}, K_d, K_{hd} gains have been calculated through equations (14–17) and (19).

Adopting this approach, the dimensional control gains used in the comparison correspond to the 16 sets of dimensionless controller parameters of Table 1 (4 PID sets, and 12 $\mathrm{PII}^{1/2}\mathrm{DD}^{1/2}$ sets).

In the tests, the rest-to-rest set-point motion with trapezoidal speed law profile is characterized by: a first phase with an acceleration of 500 rad/s^2 and a duration of 0.2 s; a second phase with a constant speed of 100 rad/s and a duration of 0.6 s; a third phase with deceleration of −500 rad/s^2 and a duration of 0.2 s. Consequently, the overall rest-to-rest duration of the motion profile is 1 s, and the overall rotation is 80 rad.

Figs. 14-17 compare the PID and $\mathrm{PII}^{1/2}\mathrm{DD}^{1/2}$ controllers for the four considered ζ-δ combinations, in terms of angular position (upper graphs) and motor torque (lower graphs). In the angular position graphs, the magenta dashed lines represent the set-point angle θ_r. In all the graphs of Figs. 14-17, as in Figs. 11 and 12, the black graphs are related to the PID, the blue graphs are related to the $\mathrm{PII}^{1/2}\mathrm{DD}^{1/2}$ with $\rho = 1$, the green graphs are related to the $\mathrm{PII}^{1/2}\mathrm{DD}^{1/2}$ with $\rho = \rho_{\max}^{1/2}$, and the red graphs are related to the $\mathrm{PII}^{1/2}\mathrm{DD}^{1/2}$ with $\rho = \rho_{\max}$. Moreover, simulation results are represented by continuous lines, while experimental results are represented by dashed lines.

Table 2 summarizes some global performance indices related to the trapezoidal velocity comparisons of Figs. 14-17: the maximum absolute

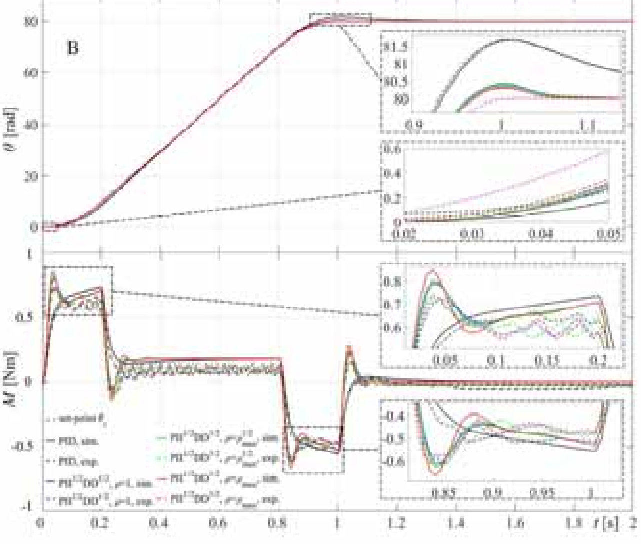

Fig. 15. Trapezoidal speed set-point, case B ($\zeta = 1.2$, $\delta = 0.02$): PID (black), $\mathrm{PII}^{1/2}\mathrm{DD}^{1/2}$ with $\rho = 1$ (blue), $\mathrm{PII}^{1/2}\mathrm{DD}^{1/2}$ with $\rho = \rho_{\max}^{1/2}$ (green), and $\mathrm{PII}^{1/2}\mathrm{DD}^{1/2}$ with $\rho = \rho_{\max}$ (red). Top: rotor angle; bottom: motor torque. Continuous lines: simulation results; dashed lines: experimental results. Magenta dashed line: set-point angle θ_r.

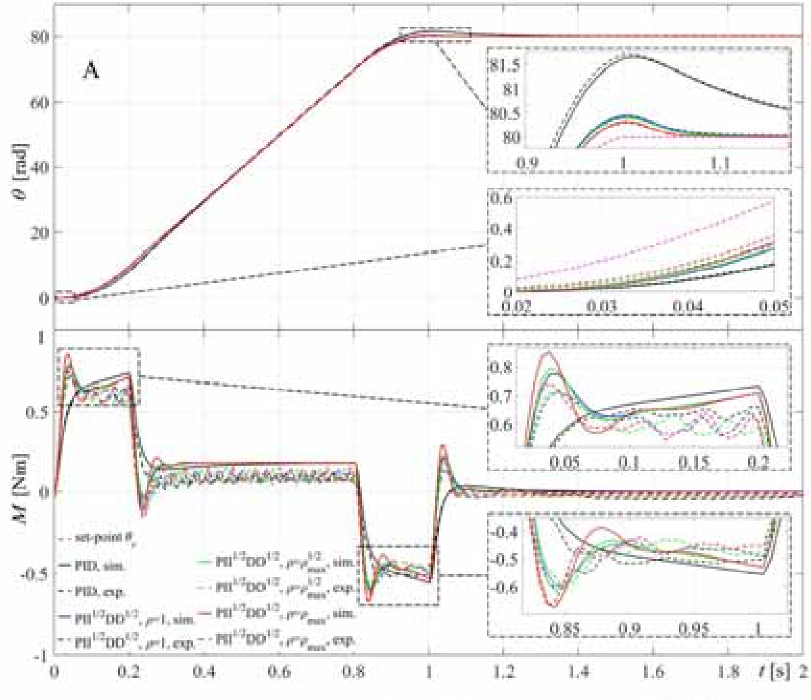

Fig. 14. Trapezoidal speed set-point, case A ($\zeta = 1.2$, $\delta = 0.01$): PID (black), $\mathrm{PII}^{1/2}\mathrm{DD}^{1/2}$ with $\rho = 1$ (blue), $\mathrm{PII}^{1/2}\mathrm{DD}^{1/2}$ with $\rho = \rho_{\max}^{1/2}$ (green), and $\mathrm{PII}^{1/2}\mathrm{DD}^{1/2}$ with $\rho = \rho_{\max}$ (red). Top: rotor angle; bottom: motor torque. Continuous lines: simulation results; dashed lines: experimental results. Magenta dashed line: set-point angle θ_r.

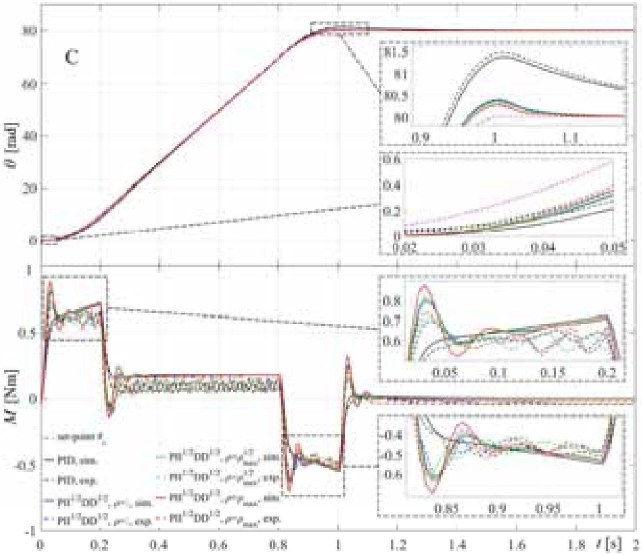

Fig. 16. Trapezoidal speed set-point, case C ($\zeta = 1.6$, $\delta = 0.01$): PID (black), $PII^{1/2}DD^{1/2}$ with $\rho = 1$ (blue), $PII^{1/2}DD^{1/2}$ with $\rho = \rho_{\max}^{1/2}$ (green), and $PII^{1/2}DD^{1/2}$ with $\rho = \rho_{\max}$ (red). Top: rotor angle; bottom: motor torque. Continuous lines: simulation results; dashed lines: experimental results. Magenta dashed line: set-point angle θ_r.

position error, $e_{\theta,\max}$; the mean absolute position error, $e_{\theta,mean}$; the maximum absolute value of the motor torque, $M_{\max}$; and the Integral Control Effort, *ICE*, defined according to the following expression:

$$ICE = \int_0^{T_{fin}} M^2 dt \simeq \sum_{i=0}^{\left[T_{fin}/T_s\right]-1} M_i^2 T_s \tag{45}$$

where $T_{fin} = 2$ s is the final time. Since in brushless DC motors, the torque is proportional to the current, the *ICE* provides a good estimation of the energy consumption.

From the observation of the graphs in Figs. 14-17 and of the values reported in Table 2, the following conclusions can be drawn:

- discrete-time simulations and experimental tests show very good agreement for the evaluation of the time histories of angular position; regarding the torque time histories, there is a good agreement in the acceleration and deceleration phases, while in the constant speed phase, the difference is higher due to the imperfect friction compensation and to the dynamics and noise of the current loop; however, in general, the experiments confirm the simulations and lead to a similar evaluation of the benefits and drawbacks of the two controllers;
- the results with the trapezoidal velocity profile confirm that the better readiness of the FO algorithm, evidenced by the continuous-time analysis in the case of step input discussed in Section 5, allows for lower tracking error in the case of a smoother motion profile;
- the reduction of the maximum absolute error $e_{\theta,\max}$ is remarkable, ranging from −71.2 % to −81.1 % in simulation and from −73.4 % to −81.3 % in the experimental tests; for all the ζ-δ combinations, the reduction of $e_{\theta,\max}$ increases for higher values of ρ;
- the decrease of the mean absolute error $e_{\theta,mean}$ is even higher and less variable in the different cases, ranging from −78.6 % to −86.0 % in simulation and from −77.5 % to −82.6 % in the experimental tests; for all the ζ-δ combinations, the reduction of $e_{\theta,mean}$ increases for higher values of ρ;
- on the other hand, the maximum absolute torque M_{max} is slightly higher for the FO controllers; the increase varies from +5.4 % to +21.6 % in simulation, but it is lower in experimental tests, ranging from +5.8 % to +13.3 %; for all the ζ-δ combinations, the maximum increase of M_{max} corresponds to $\rho = \rho_{\max}$, except for the case D;
- the *ICE* is similar for the PID and $PII^{1/2}DD^{1/2}$ controllers in simulation, with small increases for the FO algorithm with respect to the IO one, ranging between +4.3 % to +7.8 %; on the contrary, in the experimental tests the *ICEs* of the two controllers are similar, and the range of variation is between −1.3 % and +7.7 %: in case B, the $PII^{1/2}DD^{1/2}$ controller requires slightly lower control effort than the PID;
- in general, as expected, both the benefits and the drawbacks of the FO controller over the IO one are increased by higher values of ρ; the behaviour of the system with the two lower values of ρ (1 and $\rho_{\max}^{1/2}$) are very similar;
- fixing $\rho = \rho_{\max}^{1/2}$ eliminates any degree of freedom in the control design, and represents a good tuning compromise since it improves

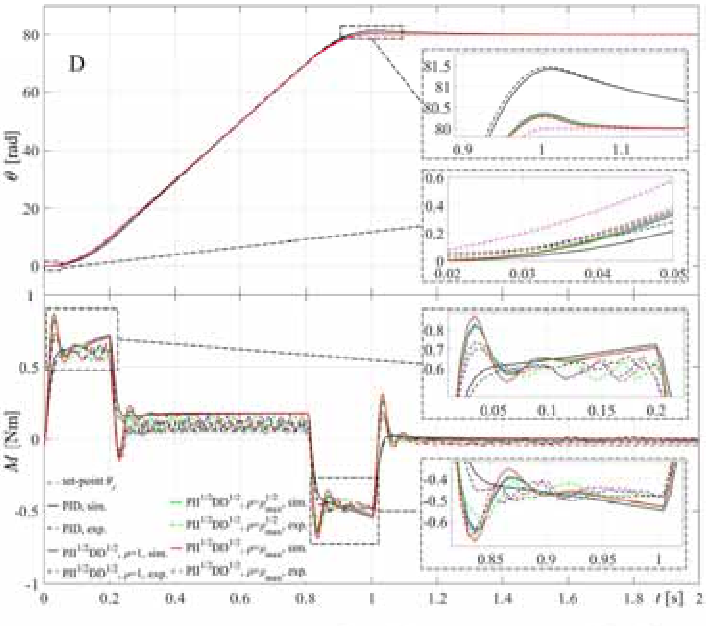

Fig. 17. Trapezoidal speed set-point, case D ($\zeta = 1.6$, $\delta = 0.02$): PID (black), $PII^{1/2}DD^{1/2}$ with $\rho = 1$ (blue), $PII^{1/2}DD^{1/2}$ with $\rho = \rho_{\max}^{1/2}$ (green), and $PII^{1/2}DD^{1/2}$ with $\rho = \rho_{\max}$ (red). Top: rotor angle; bottom: motor torque. Continuous lines: simulation results; dashed lines: experimental results. Magenta dashed line: set-point angle θ_r.

Table 2

Comparison of the PID and $\mathrm{PII}^{1/2}\mathrm{DD}^{1/2}$ controllers in the case of trapezoidal speed set-point, with the four ζ-δ combinations A, B, C, and D of Figs. 4-7; $e_{\theta,max}$: maximum absolute error; $e_{\theta,mean}$: mean absolute error; M_{max}: maximum absolute torque; *ICE:* Integral Control Effort.

ζ-δ combination, controller		$e_{\theta,\max}$ [rad]		$e_{\theta,mean}$ [rad]		M_{max} [Nm]		*ICE* [$\mathrm{N^2m^2s}$]	
		Sim.	Exp.	Sim.	Exp.	Sim.	Exp.	Sim.	Exp.
A	PID	1.6512	1.7008	0.2116	0.2587	0.7350	0.6622	0.1474	0.1240
	$\mathrm{PII}^{1/2}\mathrm{DD}^{1/2}$, $\rho = 1$	0.4539	0.4519	0.0453	0.0581	0.7745	0.7150	0.1537	0.1245
	variation w.r.t. PID	*−72.5 %*	*−73.4 %*	*−78.6 %*	*−77.5 %*	*+5.4 %*	*+8.0 %*	*+4.3 %*	*+0.4 %*
	$\mathrm{PII}^{1/2}\mathrm{DD}^{1/2}$, $\rho = (\rho_{max})^{1/2}$	0.4128	0.4130	0.0411	0.0572	0.7938	0.7122	0.1540	0.1246
	variation w.r.t. PID	*−75.0 %*	*−75.7 %*	*−80.6 %*	*−77.9 %*	*+8.0 %*	*+7.6 %*	*+4.5 %*	*+0.5 %*
	$\mathrm{PII}^{1/2}\mathrm{DD}^{1/2}$, $\rho = \rho_{max}$	0.3151	0.3174	0.0313	0.0464	0.8526	0.7461	0.1553	0.1251
	variation w.r.t. PID	*−80.9 %*	*−81.3 %*	*−85.2 %*	*−82.1 %*	*16.0 %*	*+12.7 %*	*+5.4 %*	*+0.9 %*
B	PID	1.6959	1.7032	0.2189	0.2614	0.7361	0.6657	0.1478	0.1265
	$\mathrm{PII}^{1/2}\mathrm{DD}^{1/2}$, $\rho = 1$	0.4130	0.4155	0.0414	0.0559	0.7912	0.7203	0.1542	0.1257
	variation w.r.t. PID	*−75.6 %*	*−75.6 %*	*−81.1 %*	*−78.6 %*	*+7.5 %*	*+8.2 %*	*+4.3 %*	*−0.6 %*
	$\mathrm{PII}^{1/2}\mathrm{DD}^{1/2}$, $\rho = (\rho_{max})^{1/2}$	0.3870	0.3879	0.0387	0.0568	0.8059	0.7248	0.1544	0.1264
	variation w.r.t. PID	*−77.2 %*	*−77.2 %*	*−82.3 %*	*−78.3 %*	*+9.5 %*	*+8.9 %*	*+4.5 %*	*−0.1 %*
	$\mathrm{PII}^{1/2}\mathrm{DD}^{1/2}$, $\rho = \rho_{max}$	0.3208	0.3269	0.0320	0.0456	0.8476	0.7409	0.1553	0.1249
	variation w.r.t. PID	*−81.1 %*	*−80.8 %*	*−85.4 %*	*−82.6 %*	*+15.1 %*	*+11.3 %*	*+5.1 %*	*−1.3 %*
C	PID	1.3784	1.4702	0.2066	0.2623	0.7240	0.6572	0.1431	0.1213
	$\mathrm{PII}^{1/2}\mathrm{DD}^{1/2}$, $\rho = 1$	0.3968	0.3874	0.0400	0.0554	0.8026	0.6954	0.1520	0.1263
	variation w.r.t. PID	*−71.2 %*	*−73.6 %*	*−80.6 %*	*−78.9 %*	*+10.9 %*	*+5.8 %*	*+6.2 %*	*+4.1 %*
	$\mathrm{PII}^{1/2}\mathrm{DD}^{1/2}$, $\rho = (\rho_{max})^{1/2}$	0.3664	0.3579	0.0368	0.0490	0.8223	0.7167	0.1524	0.1229
	variation w.r.t. PID	*−73.4 %*	*−75.7 %*	*−82.2 %*	*−81.3 %*	*+13.6 %*	*+9.1 %*	*+6.5 %*	*+1.3 %*
	$\mathrm{PII}^{1/2}\mathrm{DD}^{1/2}$, $\rho = \rho_{max}$	0.2909	0.2868	0.0290	0.0471	0.8806	0.7445	0.1543	0.1296
	variation w.r.t. PID	*−78.9 %*	*−80.5 %*	*−86.0 %*	*−82.0 %*	*+21.6 %*	*+13.3 %*	*+7.8 %*	*+6.8 %*
D	PID	1.4253	1.4721	0.2105	0.2403	0.7248	0.6614	0.1433	0.1180
	$\mathrm{PII}^{1/2}\mathrm{DD}^{1/2}$, $\rho = 1$	0.3610	0.3533	0.0363	0.0473	0.8222	0.7019	0.1526	0.1243
	variation w.r.t. PID	*−74.7 %*	*−76.0 %*	*−82.8 %*	*−80.3 %*	*+13.4 %*	*+6.1 %*	*+6.5 %*	*+5.3 %*
	$\mathrm{PII}^{1/2}\mathrm{DD}^{1/2}$, $\rho = (\rho_{max})^{1/2}$	0.3429	0.3340	0.0344	0.0458	0.8350	0.7382	0.1529	0.1236
	variation w.r.t. PID	*−75.9 %*	*−77.3 %*	*−83.7 %*	*−80.9 %*	*+15.2 %*	*+11.6 %*	*+6.7 %*	*+4.7 %*
	$\mathrm{PII}^{1/2}\mathrm{DD}^{1/2}$, $\rho = \rho_{max}$	0.2949	0.2933	0.0295	0.0456	0.8730	0.7348	0.1541	0.1271
	variation w.r.t. PID	*−79.3 %*	*−80.1 %*	*−86.0 %*	*−81.0 %*	*+20.4 %*	*+11.1 %*	*+7.5 %*	*+7.7 %*

accuracy while limiting the maximum increase in torque absolute value.

7. Comparison of the $\mathrm{PII}^{1/2}\mathrm{DD}^{1/2}$ and $\mathrm{PI}^{\lambda}\mathrm{D}^{\mu}$ controllers

The $\mathrm{PII}^{1/2}\mathrm{DD}^{1/2}$ and $\mathrm{PI}^{\lambda}\mathrm{D}^{\mu}$ schemes are both characterized by five tuning parameters: five gains for the $\mathrm{PII}^{1/2}\mathrm{DD}^{1/2}$, three gains and two orders for the $\mathrm{PI}^{\lambda}\mathrm{D}^{\mu}$. On the contrary, the PID has only three tuning parameters (three gains). The higher number of tuning parameters in the two FO controllers allows for achieving better control performance than the PID, but an optimization process is usually necessary. The Bode plot-based tuning method proposed in Section 3 and utilized in Sections 4-6 allows for obtaining the five $\mathrm{PII}^{1/2}\mathrm{DD}^{1/2}$ gains through direct expressions, starting from a given set of PID gains. This approach cannot be directly applied to the $\mathrm{PI}^{\lambda}\mathrm{D}^{\mu}$ scheme because, unlike the $\mathrm{PII}^{1/2}\mathrm{DD}^{1/2}$, the slopes of the low-frequency and high-frequency asymptotes of the magnitude plot are variable and depend on λ and μ.

However, a similar Bode plot-based tuning approach can be devised for the $\mathrm{PI}^{\lambda}\mathrm{D}^{\mu}$ scheme. Utilizing the differintegration operator (1), the $\mathrm{PI}^{\lambda}\mathrm{D}^{\mu}$ control is expressed in the following form:

$$u(e) = \left(K_{fp} + K_{fi}D^{-\lambda} + K_{fd}D^{\mu}\right)e \tag{46}$$

Starting from Eq. (46), it is possible to obtain the Laplace transforms of the low-frequency and high-frequency asymptotes, which are respectively K_{fi}/s^{λ} and $K_{fp} + K_{fd}s^{\mu}$. Consequently, the asymptotic magnitude slope is -20λdB/dec at low frequency and $+20\mu$dB/dec at high frequency. To extend the comparison to the $\mathrm{PI}^{\lambda}\mathrm{D}^{\mu}$ controller, the following hypotheses are imposed, coherent with the method proposed in Section 3:

- the magnitude Bode plot is symmetric with respect to the mean frequency of the given PID, $\omega_m = (\omega_{c1}\omega_{c2})^{1/2}$;
- the minimum magnitude in ω_m is equal to that of the central asymptote of the given PID, M_L;
- the low-frequency and high-frequency asymptotes intersect at (ω'_{c1}, M_H) and (ω'_{c4}, M_H).

These conditions are graphically represented in the magnitude Bode plots of Fig. 18. For the $\mathrm{PI}^{\lambda}\mathrm{D}^{\mu}$ controller:

- the first hypothesis corresponds to imposing $\lambda = \mu$ and $|K_{fi}/(j\omega_m)^{\lambda}| = |K_{fd}(j\omega_m)^{\mu}|$;
- the second hypothesis corresponds to imposing $M_L = |K_i/(j\omega_{c1})| = |K_{fp}+K_{fi}/(j\omega_m)^{\lambda}+K_{fd}(j\omega_m)^{\mu}|$;
- the third hypothesis corresponds to imposing $M_H = |K_i/(j\omega'_{c1})| = |K_{fi}/(j\omega'_{c1})^{\lambda}|$.

By elaborating algebraically these conditions, the following direct expressions of the gains K_{fp}, K_{fi}, and K_{fd} of the $\mathrm{PI}^{\lambda}\mathrm{D}^{\mu}$ controller can be obtained from the given PID gains K_p, K_i, and K_f, and from the $\mathrm{PII}^{1/2}\mathrm{DD}^{1/2}$ parameter ρ, once the fractional order λ is selected:

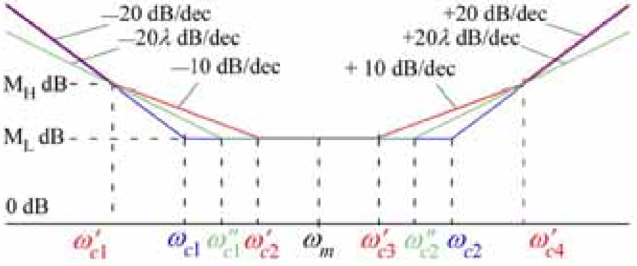

Fig. 18. Comparison of the asymptotic magnitude Bode plots of the PID (blue), $\mathrm{PII}^{1/2}\mathrm{DD}^{1/2}$ (red), and $\mathrm{PI}^{\lambda}\mathrm{D}^{\mu}$ (green) controllers.

$$
\begin{gathered}
K_{fi} = M_H \omega_{c1}^{'\lambda} \\
K_{fd} = \frac{K_{fi}}{\omega_m^{2\lambda}} \\
K_{fp} = \sqrt{M_L^2 - \left(\mathrm{Im}\left(\frac{2K_{fi}}{(j\omega_m)^{\lambda}} \right) \right)^2} - \mathrm{Re}\left(\frac{2K_{fi}}{(j\omega_m)^{\lambda}} \right)
\end{gathered}
\tag{47}
$$

with $M_L = \dfrac{2K_iK_d}{K_p - \sqrt{K_p^2 - 4K_dK_i}}$ and $M_H = \rho M_L$

This approach has been applied to the mechatronic axis utilized for the simulations and experimental tests reported in Section 6, employing the same trapezoidal speed control law. Fig. 19 shows the comparison of the PID, PII$^{1/2}$DD$^{1/2}$, and PI$^{\lambda}$D$^{\mu}$ controllers in terms of angular position (upper graphs) and motor torque (lower graphs), for the PID characterized by $\zeta = 1.2$ and $\delta = 0.01$ (case A of Sections 5 and 6). For the PII$^{1/2}$DD$^{1/2}$ controller, $\rho = \rho_{\max}^{1/2}$ is imposed, since it represents a good tuning compromise, as discussed at the end of Section 6. For the PI$^{\lambda}$D$^{\mu}$ controller, these values of λ are considered: 0.5, 0.6, 0.7, 0.8, 0.9, 1.1. For $\lambda = 1$ the PI$^{\lambda}$D$^{\mu}$ corresponds to the PID; as a matter of fact, in Fig. 19, the time histories of the PID are intermediate between those of the PI$^{\lambda}$D$^{\mu}$ controllers with $\lambda = 0.9$ and $\lambda = 1.1$. Similarly to Figs. 14-17, the magenta dashed line represents the set-point angle θ_r, simulation results are represented by continuous lines, and experimental results are represented by dashed lines.

The same comparison has been carried out also for the cases B, C, and D, with qualitatively similar results. The main global performance indices (maximum absolute position error $e_{\theta,\max}$, mean absolute position error $e_{\theta,mean}$, maximum absolute value of the torque M_{max}, and Integral Control Effort) are summarized for the four cases in Table 3. From the observation of Fig. 19 and Table 3, the following conclusions can be drawn:

- the PI$^{\lambda}$D$^{\mu}$ controller reduces the maximum absolute error $e_{\theta,\max}$ and mean absolute error $e_{\theta,mean}$ with respect to the PID for $\lambda < 1$, and the reduction is higher for lower values of λ: for $\lambda = 0.5$, the variation in $e_{\theta,\max}$ ranges from −22.5 % to −32.5 % in simulation and from −29.3 % to −36.5 % in the experimental tests, while the variation in $e_{\theta,mean}$ ranges from −40.2 % to −52.9 % in simulation and from −52.2 % to −57.0 % in the experimental tests;
- nevertheless, the error reduction with the PII$^{1/2}$DD$^{1/2}$ controller, $\rho = (\rho_{\max})^{1/2}$, is remarkably higher both in simulation and in experimental tests: the variation in $e_{\theta,\max}$ ranges from −73.4 % to −77.2 % in simulation and from −75.7 % to −77.3% in the experimental tests; the variation in $e_{\theta,mean}$ ranges from −80.6% to −83.7% in simulation and from −77.9% to −81.3% in the experimental tests;
- moreover, the error reduction with the PI$^{\lambda}$D$^{\mu}$ controller tuned with low values of λ is accompanied by a remarkable increase in maximum torque and Integral Control Effort: for $\lambda = 0.5$, the variation in M_{max} ranges from +31.0 % to +36.2 % in simulation and from +37.2 % to +43.2 % in the experimental tests, while the variation in *ICE* ranges from +29.0 % to +40.8 % in simulation and from +27.5 % to +37.4 % in the experimental tests;
- on the contrary, using the PII$^{1/2}$DD$^{1/2}$ controller with $\rho = (\rho_{\max})^{1/2}$ the increase in maximum torque and Integral Control Effort is much lower: the variation in M_{max} ranges from +8.0 % to +15.2 % in simulation and from +7.6 % to +11.6 % in the experimental tests, while the variation in *ICE* ranges from +4.5 % to +6.7 % in simulation and from −0.1 % to +4.7 % in the experimental tests;
- the considered range of λ is sufficient, since for $\lambda < 0.5$ M_{max} and *ICE* become much higher than those of the PID, while for $\lambda > 1.1$ the errors $e_{\theta,\max}$ and $e_{\theta,mean}$ become much higher than those of the PID;
- overall, the application of the proposed Bode plot-based tuning approach allows for achieving better performance in combination with the PII$^{1/2}$DD$^{1/2}$ controller rather than in combination with the PI$^{\lambda}$D$^{\mu}$ scheme.

8. Conclusions and future developments

In this paper, the comparison in position control of an inertial system between the PID and the PII$^{1/2}$DD$^{1/2}$ scheme, tuned as proposed in [44],

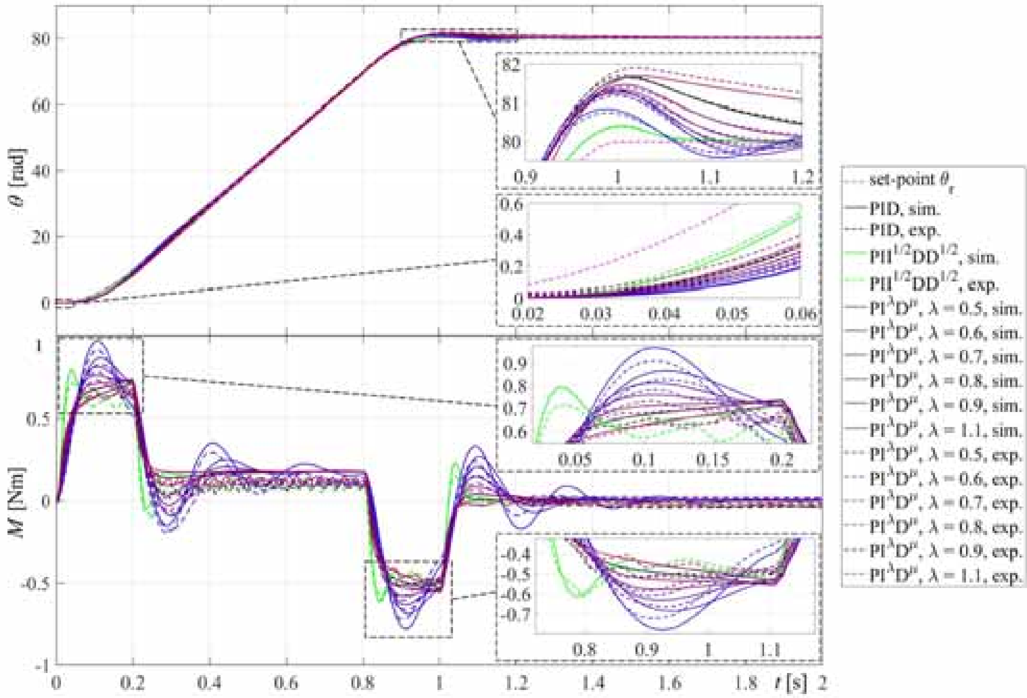

Fig. 19. Trapezoidal speed set-point, case A ($\zeta = 1.2$, $\delta = 0.01$): PID (black), PII$^{1/2}$DD$^{1/2}$ with $\rho = \rho_{\max}^{1/2}$ (green), and PI$^{\lambda}$D$^{\mu}$ with $\lambda = 0.5, 0.6, 0.7, 0.8, 0.9, 1.1$ from blue (lambda = 0.5) to red (lambda = 1.1), not to magenta. Top: rotor angle; bottom: motor torque. Continuous lines: simulation results; dashed lines: experimental results. Magenta dashed line: set-point angle θ_r.

Table 3

Comparison of the PID, $\mathrm{PII}^{1/2}\mathrm{DD}^{1/2}$, and $\mathrm{PI}^{\lambda}\mathrm{D}^{\mu}$ controllers in the case of trapezoidal speed set-point, with the A, B, C, D ζ-δ combinations of Figs. 4-6; for the $\mathrm{PII}^{1/2}\mathrm{DD}^{1/2}$ scheme, $\rho = (\rho_{max})^{1/2}$; for the $\mathrm{PI}^{\lambda}\mathrm{D}^{\mu}$ scheme, $\lambda = 0.5, 0.6, 0.7, 0.8, 0.9, 1.1$;
$e_{\theta,max}$: maximum absolute error; $e_{\theta,mean}$: mean absolute error; M_{max}: maximum absolute torque; *ICE*: Integral Control Effort.

ζ-δ combination, controller			$e_{\theta,max}$ [rad]		$e_{\theta,mean}$ [rad]		M_{max} [Nm]		*ICE* [N^{2}m^{2}s]	
			Sim.	Exp.	Sim.	Exp.	Sim.	Exp.	Sim.	Exp.
A	PID		1.6512	1.7008	0.2116	0.2587	0.7350	0.6622	0.1474	0.1240
	$\mathrm{PII}^{1/2}\mathrm{DD}^{1/2}$, $\rho = (\rho_{max})^{1/2}$		0.4128	0.4130	0.0411	0.0572	0.7938	0.7122	0.1540	0.1246
	variation w.r.t. PID		*−75.0 %*	*−75.7 %*	*−80.6 %*	*−77.9 %*	*+8.0 %*	*+7.6 %*	*+4.5 %*	*+0.5 %*
	$\mathrm{PI}^{\lambda}\mathrm{D}^{\mu}$	*λ=0.5*	1.2794	1.1977	0.1258	0.1236	0.9689	0.9110	0.2019	0.1682
		variation w.r.t. PID	*−22.5 %*	*−29.6 %*	*−40.6 %*	*−52.2 %*	*+31.1*	*+37.6*	*+37.0 %*	*+35.6 %*
		λ=0.6	1.4681	1.4439	0.1472	0.1705	0.8660	0.8259	0.1898	0.1594
		variation w.r.t. PID	*−11.1 %*	*−15.1 %*	*−30.4 %*	*−34.1 %*	*+17.8 %*	*+24.7 %*	*+28.8*	*+28.5 %*
		λ=0.7 variation	1.3327	1.2766	0.1313	0.1575	0.8114	0.7821	0.1753	0.1492
		w.r.t. PID	*−19.3 %*	*−24.9 %*	*−37.9 %*	*−39.1 %*	*+10.4 %*	*+18.1 %*	*+18.9 %*	*+20.3 %*
		λ=0.8	1.3358	1.3120	0.1321	0.1695	0.7581	0.7316	*0.1648*	0.1375
		variation w.r.t. PID	*−19.1 %*	*−22.9 %*	*−37.6 %*	*−34.5 %*	*+3.1 %*	*+10.8 %*	*+11.8 %*	*+10.8 %*
		λ=0.9	1.4662	1.4097	0.1576	0.2130	0.7356	0.6944	*0.1555*	0.1345
		variation w.r.t. PID	*−11.2 %*	*−17.1 %*	*−25.5 %*	*−17.7 %*	*+0.1 %*	*+4.9 %*	*+5.5 %*	*+8.4 %*
		λ=1.1	1.8974	1.9017	0.3952	0.4945	0.7167	0.6905	0.1361	0.1194
		variation w.r.t. PID	*+14.9 %*	*+11.8 %*	*+86.8 %*	*+91.2 %*	*−2.5 %*	*−4.3 %*	*−7.7 %*	*−3.8 %*
B	PID		1.6959	1.7032	0.2189	0.2614	0.7361	0.6657	0.1478	0.1265
	$\mathrm{PII}^{1/2}\mathrm{DD}^{1/2}$, $\rho = (\rho_{max})^{1/2}$		0.3870	0.3879	0.0387	0.0568	0.8059	0.7248	0.1544	0.1264
	variation w.r.t. PID		*−77.2 %*	*−77.2 %*	*−82.3 %*	*−78.3 %*	*+9.5 %*	*+8.9 %*	*+4.5 %*	*−0.1 %*
	$\mathrm{PI}^{\lambda}\mathrm{D}^{\mu}$	*λ=0.5*	1.2715	1.2024	0.1265	0.1216	1.0011	0.9406	0.2075	0.1704
		variation w.r.t. PID	*−23.0 %*	*−29.3 %*	*−40.2 %*	*−53.0 %*	*+36.2 %*	*+42.1 %*	*+40.8 %*	*+37.4 %*
		λ=0.6	1.5108	1.4865	0.1538	0.1711	0.8878	0.8450	0.1968	0.1643
		variation w.r.t. PID	*−8.5 %*	*−12.6 %*	*−27.3 %*	*−33.9 %*	*+20.8 %*	*+27.6 %*	*+33.5 %*	*+32.5 %*
		λ=0.7	1.5757	1.5307	0.1576	0.1937	0.8089	0.7786	0.1774	0.1502
		variation w.r.t. PID	*−4.6 %*	*−10.0 %*	*−25.5 %*	*−25.1 %*	*+10.1 %*	*+17.6 %*	*+20.3 %*	*+21.1 %*
		λ=0.8	1.5155	1.4863	0.1507	0.1847	0.7569	0.7352	0.1649	0.1376
		variation w.r.t. PID	*−8.2 %*	*−12.6 %*	*−28.8 %*	*−28.6 %*	*+3.0 %*	*+11.0 %*	*+11.9 %*	*+10.9 %*
		λ=0.9	1.5805	1.5555	0.1746	0.2344	0.7391	0.6903	0.1546	0.1315
		variation w.r.t. PID	*−4.3 %*	*−8.5 %*	*−17.5 %*	*−9.4 %*	*+0.6 %*	*+4.3 %*	*+4.9 %*	*+6.0 %*
		λ=1.1	1.9134	1.9857	0.4244	0.5335	0.7137	0.6767	0.1350	0.1165
		variation w.r.t. PID	*+15.9 %*	*+16.8 %*	*+100.6 %*	*+106.2 %*	*−2.9 %*	*+2.2 %*	*−8.5 %*	*−6.1 %*
C	PID		1.3784	1.4702	0.2066	0.2623	0.7240	0.6572	0.1431	0.1213
	$\mathrm{PII}^{1/2}\mathrm{DD}^{1/2}$, $\rho = (\rho_{max})^{1/2}$		0.3664	0.3579	0.0368	0.0490	0.8223	0.7167	0.1524	0.1229
	variation w.r.t. PID		*−73.4 %*	*−75.7 %*	*−82.2 %*	*−81.3 %*	*+13.6 %*	*+9.1 %*	*+6.5 %*	*+1.3 %*
	$\mathrm{PI}^{\lambda}\mathrm{D}^{\mu}$	*λ=0.5*	1.1284	1.0795	0.1038	0.1113	0.9631	0.9083	0.1901	0.1582
		variation w.r.t. PID	*−31.7 %*	*−36.5 %*	*−50.9 %*	*−57.0 %*	*+31.0 %*	*+37.2 %*	*+29.0 %*	*+27.5 %*
		λ=0.6	1.2675	1.2585	0.1235	0.1472	0.8474	0.8010	0.1805	0.1495
		variation w.r.t. PID	*−23.2 %*	*−26.0 %*	*−41.6 %*	*−43.1 %*	*+15.3 %*	*+21.0 %*	*+22.5 %*	*+20.5 %*
		λ=0.7	1.1433	1.1269	0.1120	0.1289	0.7839	0.7521	0.1677	0.1402
		variation w.r.t. PID	*−30.8 %*	*−33.7 %*	*−47.1 %*	*−50.2 %*	*+6.7 %*	*+13.6 %*	*+13.8 %*	*+13.1 %*
		λ=0.8	1.1540	1.1306	0.1166	0.1703	0.7246	0.7050	0.1584	1.1540
		variation w.r.t. PID	*−30.1 %*	*−33.5 %*	*−44.9 %*	*−34.2 %*	*−1.4 %*	*+6.5 %*	*+7.5 %*	*+7.1 %*
		λ=0.9	1.2521	1.2425	0.1465	0.1854	0.7280	0.6778	0.1501	0.1256
		variation w.r.t. PID	*−24.2 %*	*−26.9 %*	*−30.7 %*	*−28.3 %*	*−0.9 %*	*+2.4 %*	*+1.9 %*	*+1.2 %*
		λ=1.1	1.5852	1.4388	0.4352	0.6311	0.7026	0.6652	0.1325	0.1146
		variation w.r.t. PID	*−4.0 %*	*−15.4 %*	*+106.0 %*	*+144.0 %*	*−4.4 %*	*+0.46 %*	*−10.1 %*	*−7.6 %*
D	PID		1.4253	1.4721	0.2105	0.2403	0.7248	0.6614	0.1433	0.1180
	$\mathrm{PII}^{1/2}\mathrm{DD}^{1/2}$, $\rho = (\rho_{max})^{1/2}$		0.3429	0.3340	0.0344	0.0458	0.8350	0.7382	0.1529	0.1236
	variation w.r.t. PID		*−75.9 %*	*−77.3 %*	*−83.7 %*	*−80.9 %*	*+15.2 %*	*+11.6 %*	*+6.7 %*	*+4.7 %*
	$\mathrm{PI}^{\lambda}\mathrm{D}^{\mu}$	*λ=0.5*	1.1142	1.0792	0.0997	0.1199	1.0008	0.9481	0.1928	0.1607
		variation w.r.t. PID	*−32.5 %*	*−36.5 %*	*−52.9 %*	*−53.7 %*	*+36.2 %*	*+43.2 %*	*+30.8 %*	*+29.5 %*
		λ=0.6	1.2269	1.2087	0.1185	0.1389	0.8816	0.8461	0.1850	0.1538
		variation w.r.t. PID	*−25.7 %*	*−28.9 %*	*−44.0 %*	*−46.3 %*	*+19.9 %*	*+27.8 %*	*+25.5 %*	*+24.0 %*
		λ=0.7	1.3973	1.3756	0.1382	0.1677	0.7771	0.7456	0.1690	0.1407
		variation w.r.t. PID	*−15.4 %*	*−19.1 %*	*−34.7 %*	*−35.2 %*	*+5.7 %*	*+12.7 %*	*+14.6 %*	*+13.4 %*
		λ=0.8	1.3291	1.3043	0.1374	0.2046	0.7291	0.6965	0.1581	0.1340
		variation w.r.t. PID	*−19.5 %*	*−23.3 %*	*−35.1 %*	*−20.9 %*	*−0.8 %*	*+5.2 %*	*+7.2 %*	*+8.0 %*
		λ=0.9	1.3641	1.3819	0.1671	0.1904	0.7297	0.6658	0.1491	0.1232
		variation w.r.t. PID	*−17.4 %*	*−18.7 %*	*−21.0 %*	*−26.4 %*	*−0.7 %*	*+0.5 %*	*+1.1 %*	*−0.7 %*
		λ=1.1	1.6025	1.4814	0.4490	0.7400	0.6994	0.6741	0.1313	0.1123
		variation w.r.t. PID	*−2.9 %*	*−12.9 %*	*+112.2 %*	*+186.1 %*	*−4.9 %*	*1.8 %*	*−10.9 %*	*−9.4 %*

has been generalized by adopting the nondimensional formulation discussed in Section 4. In this formulation, a frictionless model is considered (Fig. 2, Eq. (20)), to minimize the number of dimensionless parameters. Consequently, in the experimental setup, friction has been compensated using a feedforward term, differently from the tests reported in [44].

The nondimensional 3D graphs of Figs. 4-7 represent the comparison of the two controllers in terms of settling time, rise time, and overshoot in the presence of step input, and phase margin. These 3D surfaces are functions of the dimensionless parameters ζ and δ, which correspond to the derivative and integral PID gains. Using these maps, it is possible to evaluate the convenience of replacing a given PID with the corresponding $\mathrm{PII}^{1/2}\mathrm{DD}^{1/2}$ controller depending on the magnitude of the integral and derivative terms.

The 3D graphs of Figs. 4-7 are obtained by continuous time simulations, and FO derivatives and integrals are calculated taking into account the complete time history of the error. In real-time mechatronic applications, FO derivatives and integrals must be calculated in discrete-time by finite-order digital filters, considering only the recent past of the error. Moreover, even if the step input response provides useful indications for the behaviour of linear systems, smoother profiles are used for position control to limit motion discontinuities, torque peaks, and consequent vibrational phenomena. To overcome these limitations, the $PII^{1/2}DD^{1/2}$ controller has been applied to a real system, replacing the PID controller in case of tunings characterized by ζ-δ values for which the FO scheme exhibits better readiness in the continuous-time step response.

Discrete-time simulations and experimental results indicate that the better readiness of the $PII^{1/2}DD^{1/2}$ controller with the proposed tuning results in a reduction of the tracking error also in real conditions, with a smoother motion profile and calculating the FO terms using a 6th-order digital filter, with a limited computational burden. The decreases of the maximum and mean absolute errors are remarkable (respectively −73 % ÷ −81 % and −79 % ÷ −86 % in experimental tests, depending on the considered ζ-δ case). This accuracy improvement is obtained with a limited increase of the maximum peak torque (+6 % ÷ +13 %, depending on the ζ-δ combination) and with comparable Integral Control Effort (−1 % ÷ +8 %).

To extend the comparison to the $PI^{\lambda}D^{\mu}$ controller, the proposed Bode plot-based tuning method has been adapted to this scheme, as discussed in Section 7. Simulations and experimental tests demonstrate that while both FO controllers can achieve better performance compared to the PID, the proposed method yields superior results when combined with the $PII^{1/2}DD^{1/2}$ scheme rather than the $PI^{\lambda}D^{\mu}$ scheme, since it realizes higher error reduction with lower increases in peak torque and Integral Control Effort.

Overall, the results show that the proposed $PII^{1/2}DD^{1/2}$ scheme and tuning approach is an interesting and almost cost-free solution to improve the performance of position control, without requiring significant hardware upgrades on commercial motion control systems. The method can be offered as a simple add-on software option to commercial PID controllers, and the end-users can select this fractional-order upgrade starting from an existing set of PID parameters.

The evaluation of the performance benefits is general, thanks to the nondimensional approach presented in Section 4 and used for the results outlined in Section 5. Consequently, it is possible to evaluate the benefits and drawbacks of switching from PID to $PII^{1/2}DD^{1/2}$ directly from the 3D maps of Section 4 (Figs. 4–7). To enhance the utility of this work, the data represented in these 3D maps are provided to end-users through the available .FIG files (see supplementary materials).

In future work, the proposed FO scheme will be applied not only to a single axis with direct drive but also to machines equipped with ordinary [51] or planetary gears [52,53], to evaluate the behaviour of the controller in the presence of backlash and elasticity of the transmission.

CRediT authorship contribution statement

Luca Bruzzone: Conceptualization, Methodology, Writing – original draft, Writing – review & editing. **Chiara Micheli:** Investigation, Software, Visualization, Validation, Writing – review & editing.

Declaration of competing interest

The authors declare that they have no known competing financial interests or personal relationships that could have appeared to influence the work reported in this paper.

Data availability

The 3D maps of Figs. 4-7 and the plots of Figs. 8-12, 14-17, and 19 are available in form of .FIG files as supplementary material.

Acknowledgment

The authors gratefully acknowledge the support provided by the University of Genoa.

Supplementary materials

Supplementary material associated with this article can be found, in the online version, at doi:10.1016/j.mechatronics.2024.103169.

References

[1] Miller KS, Ross B. An introduction to the fractional calculus and fractional differential equations. New York, NY, USA: John Wiley & Sons; 1993.
[2] Das S. Functional fractional calculus. Berlin/Heidelberg, Germany: Springer-Verlag; 2011.
[3] Hilfer R. Applications of fractional calculus in physics. Singapore: World Scientific; 2000.
[4] Atanacković TM, Pilipović S, Stanković B, Zorica D. Fractional calculus with applications in mechanics: wave propagation, impact and variational principles. New Jersey, NY, USA: Wiley; 2014.
[5] Rihan FA. Numerical Modeling of Fractional-Order Biological Systems. Abstr Appl Anal 2013;2013:816803.
[6] Sasso M, Palmieri G, Amodio D. Application of fractional derivative models in linear viscoelastic problems. Mech Time-Dependent Mater 2011;15:367–87.
[7] Kozioł K, Stanisławski R, Bialic G. Fractional-Order SIR Epidemic Model for Transmission Prediction of COVID-19 Disease. Appl Sci 2020;10:8316.
[8] Podlubny I. Fractional-order systems and $PI^{\lambda}D^{\mu}$ controllers. IEEE Trans Autom Control 1999;44:208–13.
[9] Shah P, Agashe S. Review of fractional PID controller. Mechatronics 2016;38: 29–41.
[10] Beschi M, Padula F, Visioli A. The generalised isodamping approach for robust fractional PID controllers design. Int J Control 2015;90:1157–64.
[11] Yeroglu C, Tan N. Note on fractional-order proportional-integral-differential controller design. IET Control Theory Appl 2012;5:1978–89.
[12] Norsahperi NMH, Danapalasingam KA. Particle swarm-based and neuro-based FOPID controllers for a Twin Rotor System with improved tracking performance and energy reduction. ISA Trans 2020;102:230–44. https://doi.org/10.1016/j.isatra.2020.03.001.
[13] Kesarkar AA, Selvaganesan N. Tuning of optimal fractional-order PID controller using an artificial bee colony algorithm. Syst Sci Control Eng 2015;3:99–105.
[14] Oshnoei A, Khezri R, Muyeen SM, Blaabjerg F. On the Contribution of Wind Farms in Automatic Generation Control. Review and New Control Approach Appl Sci 2018;8:1848.
[15] Saidi B, Amairi M, Najar S, Aoun M. Bode shaping-based design methods of a fractional order PID controller for uncertain systems. Nonlinear Dyn 2015;80: 1817–38.
[16] Tufenkci S, Alagoz BB. An overview of FOPID controller design in s-domain: design methodologies and robust controller performance. Int J Syst Sci 2023;54:2316–36.
[17] Dimeas I, Petras I, Psychalinos C. New analog implementation technique for fractional-order controller: a DC motor control. AEU Int J Electron Commun 2017; 78:192–200.
[18] Haji V, Monje C. Fractional-order PID control of a chopper-fed DC motor drive using a novel firefly algorithm with dynamic control mechanism. Soft Comput 2018;22:6135–46.
[19] Hekimoglu B. Optimal Tuning of Fractional Order PID Controller for DC Motor Speed Control via Chaotic Atom Search Optimization Algorithm. IEEE Access 2019; 7:38100–14.
[20] Puangdownreong D. Fractional order PID controller design for DC motor speed control system via flower pollination algorithm. Trans Electr Eng Electron Commun 2019;17:14–23.
[21] Viola J, Angel L, Sebastian JM. Design and robust performance evaluation of a Fractional Order PID controller applied to a DC Motor. IEEE/CAA J Autom Sin 2017;4:304–14.
[22] Olejnik P, Adamski P, Batory D, Awrejcewicz J. Adaptive Tracking PID and FOPID Speed Control of an Elastically Attached Load Driven by a DC Motor at Almost Step Disturbance of Loading Torque and Parametric Excitation. Appl Sci 2021;11:679.
[23] Zheng W, Luo Y, Pi Y, Chen Y. Improved frequency-domain design method for the fractional order proportional-integral-derivative controller optimal design: a case study of permanent magnet synchronous motor speed control. IET Control Theory Appl 2018;12:2478–87.
[24] Chen P, Luo Y. A Two-Degree-of-Freedom Controller Design Satisfying Separation Principle With Fractional-Order PD and Generalized ESO. IEEE ASME Trans Mechatron 2022;27:137–48.
[25] Sun G, Ma Z, Yu J. Discrete-Time Fractional Order Terminal Sliding Mode Tracking Control for Linear Motor. IEEE Trans Ind Electron 2018;65:3386–94.
[26] Chen SY, Li TH, Chang CH. Intelligent fractional-order backstepping control for an ironless linear synchronous motor with uncertain nonlinear dynamics. ISA Trans 2019;89:218–32.
[27] Lino P, Maione G. Cascade Fractional-Order PI Control of a Linear Positioning System. IFAC PapersOnLine 2018;51:557–62.

[28] Yao B, Al-Majed M, Tomizuka M. High-Performance Robust Motion Control of Machine Tools: an Adaptive Robust Control Approach and Comparative Experiments. IEEE ASME Trans Mechatron 1997;2:63–76.

[29] Yao B, Jiang C. Advanced Motion Control: from Classical PID to Nonlinear Adaptive Robust Control. In: Proceedings of the 11th IEEE International Workshop on Advanced Motion Control; 2010. p. 815–29. https://doi.org/10.1109/AMC.2010.5464026. 21-24 March.

[30] Lu L, Yao B, Wang Q, Chen Z. Adaptive robust control of linear motors with dynamic friction compensation using modified LuGre model. Automatica 2009;45:2890–6.

[31] Wang Z, Wang X, Xia J, Shen H, Meng B. Adaptive sliding mode output tracking control based-FODOB for a class of uncertain fractional-order nonlinear time-delayed systems. Sci China Technol Sci 2020;63:1854–62. https://doi.org/10.1007/s11431-019-1476-4.

[32] Zhang S, Li Z, Wang H-N, Xiong T. Fractional order sliding mode control based on single parameter adaptive law for nano-positioning of piezoelectric actuators. IET Control Theory Appl 2021;15:1422–37.

[33] Ren HP, Jiao S-S, Wang X, Kaynak O. Fractional Order Integral Sliding Mode Controller Based on Neural Network: theory and Electro-Hydraulic Benchmark Test. IEEE ASME Trans Mechatron 2022;27:1457–66.

[34] Han S. Grey Wolf and Weighted Whale Algorithm Optimized IT2 Fuzzy Sliding Mode Backstepping Control with Fractional-Order Command Filter for a Nonlinear Dynamic System. Appl Sci 2021;11:489.

[35] Sui S, Tong S. FTC Design for Switched Fractional-Order Nonlinear Systems: an Application in a Permanent Magnet Synchronous Motor System. IEEE Trans Cybern 2023;53:2506–15.

[36] Yang Z, Wang D, Sun X, Wu J. Speed sensorless control of a bearingless induction motor with combined neural network and fractional sliding mode. Mechatronics 2022;82:102721.

[37] Hammouche S, Mansouri R, Maidi A, Bettayeb M. New fractional-order LADRC scheme based on a novel filtered Bode's ideal transfer function for integer-order systems. Mechatronics 2023;93:103004.

[38] Sebastian A, Karbasizadeh N, Saikumar N, HosseinNia H. Augmented Fractional-order Reset Control: application in Precision Mechatronics. In: Proceedings of the 2021 IEEE/ASME International Conference on Advanced Intelligent Mechatronics (AIM); 2021. p. 231–8. https://doi.org/10.1109/AIM46487.2021.9517368. 12–16 July.

[39] Zhong Y, Gao J, Zhang L. Fractional-order feedforward control method for permanent magnet linear synchronous motor based on frequency-domain adjustment theory. Mech Syst Signal Process 2023;190:110115.

[40] Bruzzone L, Bozzini G. $PDD^{1/2}$ control of purely inertial systems: nondimensional analysis of the ramp response. In: Proceedings of the 30th IASTED International Conference Modelling, Identification, and Control (MIC 2011); 2011. p. 308–15. https://doi.org/10.2316/P.2011.718-056. 14–16 February.

[41] Bruzzone L, Fanghella P. Comparison of $PDD^{1/2}$ and PD^{β} position controls of a second order linear system. In: Proceedings of the 33rd IASTED International Conference on Modelling, Identification and Control (MIC 2014); 2014. p. 182–8. https://doi.org/10.2316/P.2014.809-043. 17–19 February.

[42] Bruzzone L, Fanghella P. Fractional-order control of a micrometric linear axis. J Control Sci Eng 2013;2013:947428. https://doi.org/10.1155/2013/947428.

[43] Bruzzone L, Fanghella P, Baggetta M. Experimental assessment of fractional-order $PDD^{1/2}$ control of a brushless DC motor with inertial load. Actuators 2020;9(1):13. https://doi.org/10.3390/act9010013.

[44] Bruzzone L, Baggetta M, Fanghella P. Fractional-Order $PII^{1/2}DD^{1/2}$ Control: theoretical Aspects and Application to a Mechatronic Axis. Appl Sci 2021;11(8):3631. https://doi.org/10.3390/app11083631.

[45] Jakovljevic BB, Sekara TB, Rapaic MR, Jelicic ZD. On the distributed order PID controller. Int J Electron Commun 2017;79:94–101. https://doi.org/10.1016/j.aeue.2017.05.036.

[46] Dastjerdi AA, Saikumar N, HosseinNia SH. Tuning guidelines for fractional order PID controllers: rules of thumb. Mechatronics 2018;56:26–36.

[47] Podlubny I. Fractional differential equations. New York, NY, USA: Academic Press; 1999.

[48] Machado JT. Fractional-order derivative approximations in discrete-time control systems. J Syst Anal Model Simul 1999;34:419–34.

[49] Chen YQ, Petras I, Xue D. Fractional Order Control—A Tutorial. In: Proceedings of the 2009 American Control Conference; 2009. p. 1397–411. 10–12 June.

[50] Monje CA, Chen YQ, Vinagre BM, Xue D, Feliu V. Fractional Order systems and controls. London, UK: Springer-Verlag; 2010.

[51] Concli F, Gorla C, Stahl K, Hoehn B-R, Stemplinger J-P, Schultheiss H. Load independent power losses of ordinary gears: numerical and experimental analysis. In: Proceedings of 5th World Tribology Congress, WTC 20132; 2013. p. 1243–6. 8–13 September.

[52] Bilancia P, Monari L, Raffaeli R, Peruzzini M, Pellicciari M. Accurate transmission performance evaluation of servo-mechanisms for robots. Robot Comput Integr Manuf 2022;78:102400. https://doi.org/10.1016/j.rcim.2022.102400.

[53] Fanghella P, Bruzzone L, Ellero S, Landò R. Kinematics, efficiency and dynamic balancing of a planetary gear train based on nutating bevel gears. Mech Based Des Struct Mach 2016;44(1–2):72–85. https://doi.org/10.1080/15397734.2015.1047956.

Luca Bruzzone Graduated with first-class honours in Mechanical Engineering in 1997, with a specialisation in Industrial Automation and Robotics. From March 1998 he was mechanical and structural designer (finite element method) of machines for handling of bulk materials and containers in the Material Handling division of Techint Italimpianti. From 1999 to 2017 he was Assistant Professor at the University of Genoaa within the SSD ING-IND-13 (Mechanics of Machinery). Since 2017 he has been Associate Professor at the same University, within the same SSD. His research activity is mainly focussed on the following themes: parallel robotics (kinematic analysis, singularity analysis, design, prototyping, impedance control); modular robotics (design, prototyping); minirobotic devices and microgrippers with flexible joints (design, prototyping); design of statically-balanced robotic architectures with high energetic efficiency; application of fractional calculus to control of mechatronic devices; ground mobile robotics for surveillance and inspection (design, prototyping); mechanical design of wave energy converters. He is now Coordinator of the Laurea Degree Course in Mechanical Engineering, Automation and Mechatronic curriculum at the University of Genoa.

Chiara Micheli was born in La Spezia, Italy in 1997. She received the M.S. degree in Mechanical Engineering - curriculum Mechatronics, from the University of Genoa, Genoa, Italy, in 2021. She is currently a Ph.D student at University of Genoa in Science and Technologies for electronics and telecommunication engineering. She is working on robotic systems based on tactile sensing for biomedical applications.